

Graphical abstract



Correspondence

In brief

Highlights

- 

Article

A heart-brain-spleen axis controls cardiac remodeling to hypertensive stress

Sara Perrotta,¹ Lorenzo Carnevale,¹ Marialuisa Perrotta,^{1,2} Fabio Pallante,¹ Tomasz P. Mikołajczyk,³ Valentina Fardella,¹ Agnese Migliaccio,¹ Stefania Fardella,¹ Sara Nejat,⁴ Bogusław Kapelak,⁵ Azzurra Zonfrilli,² Jacopo Pacella,¹ Francesco Mastroiacovo,¹ Raimondo Carnevale,¹ Calum Bain,⁶ Sarah Lena Puhl,^{7,8} Giuseppe D'Agostino,^{9,10} Slava Epelman,^{4,12} Tomasz J. Guzik,^{3,11} Giuseppe Lembo,^{1,2} and Daniela Carnevale^{1,13,14,*}

¹Department of Angiocardioneurology and Translational Medicine, IRCCS Neuromed, Pozzilli, Italy

²Department of Molecular Medicine, "Sapienza" University of Rome, Rome, Italy

³Department of Internal and Agricultural Medicine and Centre for Medical Genomics Omicron, Jagiellonian University, Collegium Medicum, Kraków, Poland

⁴Toronto General Hospital Research Institute, University Health Network (UHN), Toronto, ON, Canada

⁵Department of Cardiac Surgery and Transplantation, Jagiellonian University, Collegium Medicum, Kraków, Poland

⁶Centre for Inflammation Research, Institute for Regeneration and Repair, University of Edinburgh, Edinburgh, UK

⁷Comprehensive Heart Failure Center, Department of Translational Research, University Clinic Wuerzburg, Wuerzburg, Germany

⁸Institute for Cardiovascular Prevention (IPEK), Ludwig-Maximilians-Universität (LMU) Munich, Munich, Germany

⁹Faculty of Biology, Medicine and Health, University of Manchester, Manchester, UK

¹⁰Lydia Becker Institute of Immunology and Inflammation, University of Manchester, Manchester, UK

¹¹Centre for Cardiovascular Science, University of Edinburgh, Edinburgh, UK

¹²Ted Rogers Centre for Heart Research, Translational Biology and Engineering Program, Department of Immunology, University of Toronto, Peter Munk Cardiac Centre, UHN, Toronto, ON, Canada

¹³Department of Medical-Surgical Sciences and Biotechnologies, "Sapienza" University of Rome, Latina, Italy

¹⁴Lead contact

*Correspondence: daniela.carnevale@neuromed.it

<https://doi.org/10.1016/j.immuni.2025.02.013>

SUMMARY

Hypertensive heart disease (HTN-HD) meaningfully contributes to hypertension morbidity and mortality. Initially established as an adaptive response, HTN-HD progresses toward worsening of left ventricle (LV) function and heart failure (HF). Hypertensive stress elevates sympathetic nervous system (SNS) activity, a negative clinical predictor, and expands macrophages. How they interact in the compensatory phase of HTN-HD is unclear. We report that LV pressure overload recruited a brainstem neural circuit to enhance splenic SNS and induce placental growth factor (PIGF) secretion. During hypertensive stress, PIGF drove the proliferation of self-renewing cardiac resident macrophages (RMs) expressing its receptor neuropilin-1 (NRP1). Inhibition of the splenic neuroimmune axis or ablation of NRP1 in RM hindered the adaptive response to hypertensive stress, leading to HF. In humans, circulating PIGF correlated with cardiac hypertrophy, and failing hearts expressed NRP1 in RMs. Here, we discovered a multiorgan response driving a neural reflex to expand cardiac NRP1+ RM and counteract HF.

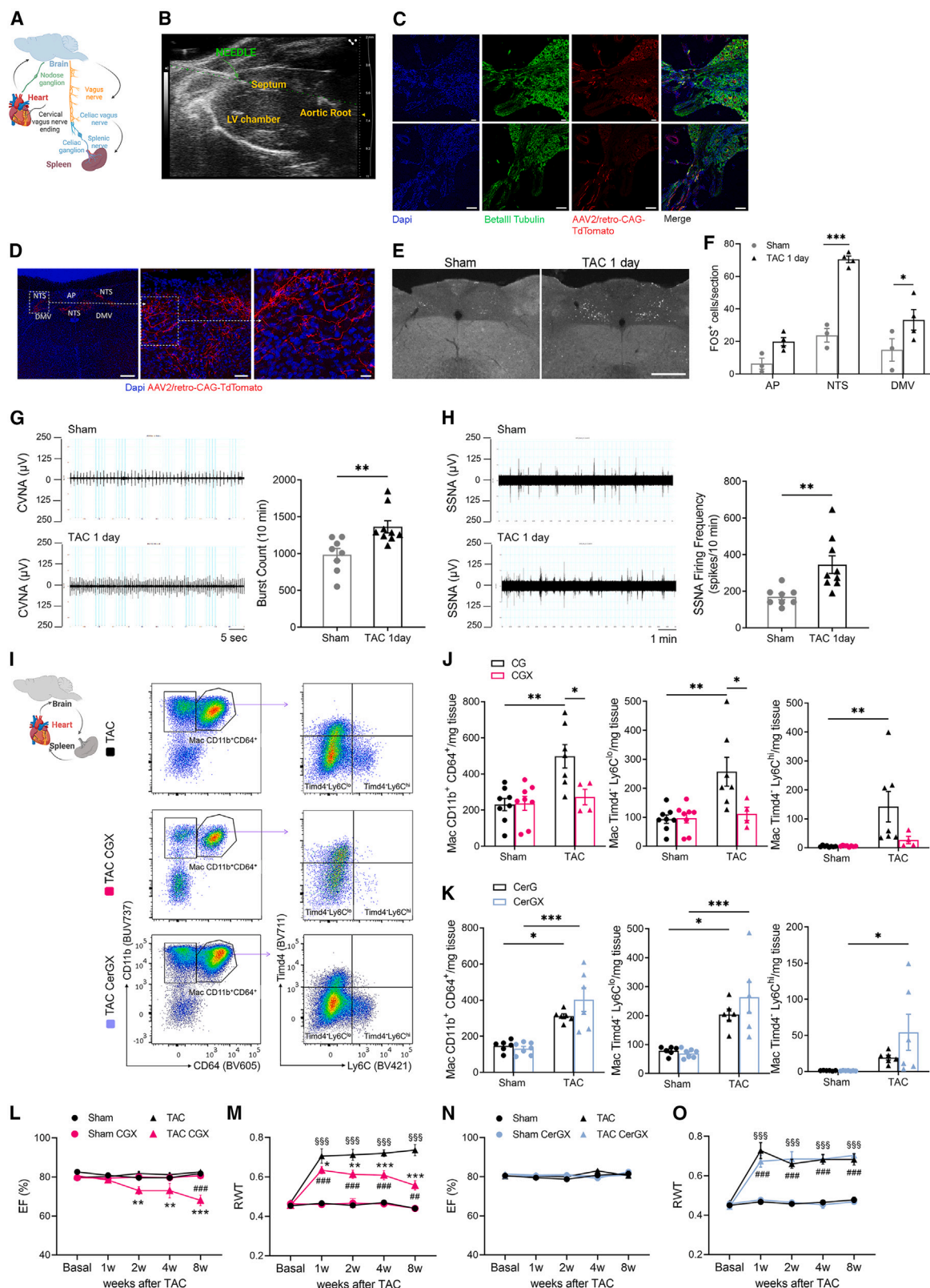
INTRODUCTION

Hypertension is a common disorder, impacting public health by increasing cardiovascular risk.^{1,2} Development of hypertensive heart disease (HTN-HD) is an important contributor to hypertension-related morbidity and mortality.^{3–5} Established as a consequence of chronic left ventricle (LV) overload, HTN-HD may evolve into heart failure (HF). Typically accompanied by neurohormonal hyperactivation, the initial adaptive LV remodeling normalizes the mechanical stress, preserving cardiac function.^{6,7} However, HTN-HD slowly develops, leading to an impairment of LV relaxation in response to diastolic filling, usually recognized as increased LV stiffness and, in the long term, depressed LV function or HF.⁸

Mechanisms that lead to HF involve numerous pathways, identified as neurohormonal imbalance, autonomic nervous system (ANS) dysregulation, and exacerbated or inadequate immune response.^{9–12} However, how the heart may succeed in counteracting the progression toward HF is still the object of investigation.

Experimental models can reproduce this diffuse clinical condition to help unravel adaptive and maladaptive mechanisms underlying LV remodeling. In mice, the surgical transverse aortic constriction (TAC)—a mechanical model of pressure overload—is characterized by an initial adaptive remodeling that decreases LV stiffness and preserves function over time.^{13–15} Our group has shown that placental growth factor (PIGF) is involved in the LV adaptive response to chronic pressure overload,





(legend on next page)

whereby the absence of PIGF hampers the establishment of adaptive cardiac hypertrophy, leading to a rapid development of HF upon pressure overload.¹⁴ In a different model of angiotensin II-induced HTN-HD, it has been shown that the LV response is dictated by a fine balance between resident and recruited macrophages.^{16,17} Recent studies have revealed that cardiac resident macrophages (RMs) organize adaptive remodeling to pressure overload by sensing mechanical stimuli,¹⁸ modulating fibrosis, and promoting angiogenesis.¹⁹ Other reports have shown that also monocyte-derived macrophages infiltrate the heart early during pressure overload, and blocking this response mitigates late pathological LV remodeling.²⁰

Cardiac remodeling to hypertension is, in part, controlled by distant organs. We and others have shown that the spleen is crucial for establishing immune responses in cardiovascular disease.^{21–23} Both deleterious and beneficial functions of splenic-mediated immune responses have been identified, suggesting the need for further investigations. Our previous data defined PIGF as a neuro-immune mediator released in response to splenic noradrenergic activation,^{24,25} suggesting the participation of the nervous system in the multiorgan complexity. Here, we have revealed that the adaptation to LV pressure overload requires a coordinated multiorgan response involving the heart, the nervous, and the immune systems. We identified the sympathetic nervous system (SNS)-mediated splenic production of PIGF as a cardioprotective factor that led to the expansion of a specific subset of cardiac macrophages expressing its receptor neuropilin-1 (NRP1). The interruption of this cardioprotective neural reflex by denervation or removal of the spleen, or by genetic ablation of NRP1 in cardiac RM, impaired the adaptive cardiac remodeling and led to HF. In hypertensive humans, circulating PIGF amounts were significantly increased and correlated with hypertrophic remodeling. Also, NRP1 was expressed by a subset of cardiac RM, indicating that the PIGF-NRP1 axis is conserved in the failing human heart.

RESULTS

Pressure overload induces LV adaptive remodeling and macrophage expansion

C57BL/6J wild-type (WT) mice subjected to pressure overload established an early adaptive LV hypertrophy, which was maintained over time (Figure S1A).^{14,26} The process of concentric cardiac re-

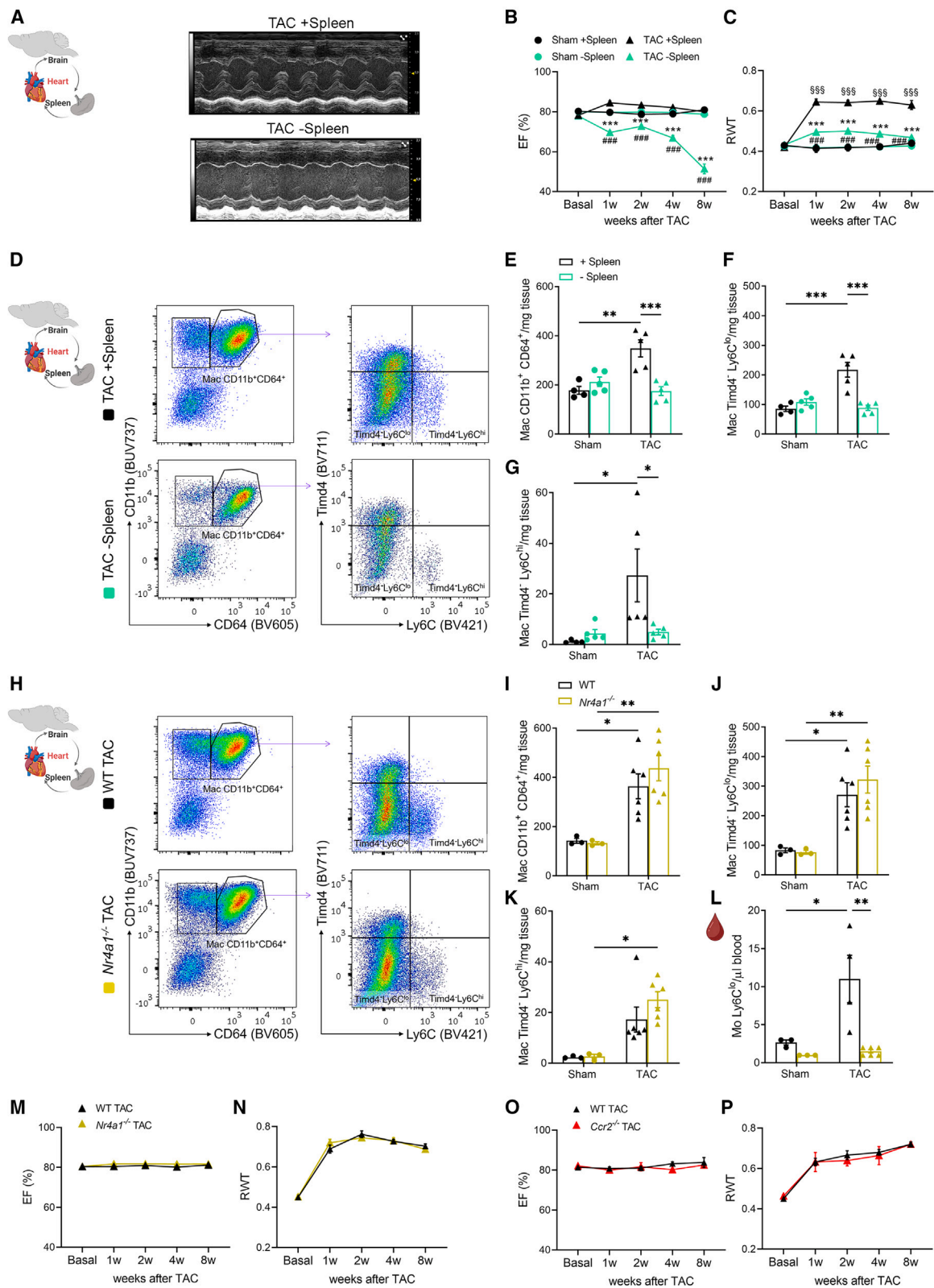
modeling reached the peak of end-diastolic LV posterior wall (LVPW;d) and intraventricular septum (IVS;d) hypertrophy and end-diastolic LV internal diameter (LVID;d) reduction 1 week after TAC, as reflected by the elevation in the relative wall thickness (RWT) index (Figures S1B and S1C). LV function was preserved until later stages—8 weeks after TAC (Figures S1B and S1C). The flow cytometry gating strategy shown in Figure S2 was used to parse the LV monocytes and macrophages 4 days after TAC, an early time point preceding the establishment of LV adaptive hypertrophy. TAC induced an expansion of CD45⁺ leukocytes (Figures S3A and S3B), characterized by a significant increase in CD11b⁺CD64[−] cells (Figures S3A and S3C) and CD11b⁺CD64⁺ macrophages (Figures S3A and S3F), consistent with previous literature.^{18,19,27} We further stratified CD11b⁺CD64[−] cells by the expression of the lymphocyte antigen 6 complex locus C1 (Ly6C) (Figure S2). 4 days of pressure overload significantly increased both Ly6C^{hi} and Ly6C^{lo} monocyte subsets characterized by proinflammatory and patrolling/reparative functions, respectively (Figures S3D and S3E). Cardiac macrophages were characterized based on the expression of the phosphatidylserine receptor Timd4 as well as Ly6C, used as a surrogate marker for recently recruited C–C chemokine receptor type 2 (CCR2⁺) macrophages¹⁷ (Figure S2), to distinguish Timd4⁺Ly6C^{lo} RM expanding by local proliferation, Timd4[−]Ly6C^{lo} RM expanding by local proliferation and/or replenishment by recruited cells, and Timd4[−]Ly6C^{hi} macrophages exclusively replenished by recruited cells.^{16,28} We found unchanged amounts of Timd4⁺Ly6C^{lo} RM (Figure S3G), a significant numerical expansion of Timd4[−]Ly6C^{lo} RM (Figure S3H), and a significantly increased number of Timd4[−]Ly6C^{hi} recruited macrophages (Figure S3I).

The LV establishes a neural circuit with the dorsal vagal complex in the brain

Increasing data imply that peripheral immune responses are influenced by the brain,^{29,30} yet it remains still unknown how the brain perceives HTN-HD. We analyzed the neural circuits that the heart establishes to inform the brain of pathological cardiac challenges (Figure 1A). To achieve this aim, we took advantage of retrograde viruses to track neuronal connections between the LV and the brain. AAV2/retro-CAG-TdTomato (AAV2, Adeno-associated virus 2) was delivered in the LV walls of WT mice at the steady state via non-invasive ultrasound-guided injections (Figure 1B).

Figure 1. A neural circuit connecting heart-brain-spleen hampers HF

(A) Schematics of the heart-brain-spleen axis.
(B–D) Ultrasound-guided injection of AAV2/retro-CAG-TdTomato virus in the LV (B) and visualization in the nodose ganglion (scale bars, 50 μ m, 100 μ m) recognized by staining BetalIII tubulin+ neurons (green) (C) and in nucleus of the solitary tract (NTS), area postrema (AP), and dorsal motor nucleus of the vagus nerve (DMV) (scale bars, 200, 100, 20 μ m) (D).
(E and F) Visualization (E) and quantification (F) of FOS⁺ neurons in the AP, NTS, and DMV (scale bar, 500 μ m). $n = 3$ sham; $n = 4$ TAC. Data as mean \pm SEM and analyzed by two-way ANOVA and Sidak post hoc. * $p < 0.05$, *** $p < 0.001$.
(G and H) CVNA (G) and SSNA (H) raw signals in 1-day TAC and sham mice and quantification. $n = 8$ sham; $n = 9$ TAC. Data as mean \pm SEM and analyzed by unpaired t test. ** $p < 0.01$.
(I) Flow cytometry of LV macrophages (Mac) in TAC, CGX, CerGX, or control mice.
(J and K) Quantification of LV total CD11b⁺CD64⁺ Mac, Timd4[−]Ly6C^{lo} RMs, and Timd4[−]Ly6C^{hi} recruited Mac in sham and TAC mice subjected to CGX (J) or CerGX (K) or control procedures. $n = 8$ sham CG; $n = 7$ TAC CG; $n = 8$ sham CGX; $n = 4$ TAC CGX. $n = 6$ sham CerG; $n = 6$ TAC CerG; $n = 7$ sham CerGX; $n = 6$ TAC CerGX. Data as mean \pm SEM and analyzed by two-way ANOVA and Tukey post hoc. * $p < 0.05$, ** $p < 0.01$, *** $p < 0.001$.
(L–O) Serial LV echocardiography in basal condition and at 1–2–4–8 weeks after TAC in mice with CGX (L and M) or CerGX (N and O). EF and RWT are shown. $n = 5$ sham; $n = 5$ TAC; $n = 3$ sham CGX; $n = 7$ TAC CGX. $n = 4$ sham; $n = 4$ TAC; $n = 4$ sham CerGX; $n = 6$ TAC CerGX. Data as mean \pm SEM and analyzed by two-way ANOVA and Tukey post hoc. §§§ $p < 0.001$ sham vs. TAC; ## $p < 0.01$, ### $p < 0.001$ TAC CGX or TAC CerGX vs. their respective sham; * $p < 0.05$, ** $p < 0.01$, *** $p < 0.001$ TAC vs. TAC CGX or TAC CerGX. Schematics were created with BioRender.com.
See also Figures S1–S5 and Table S1.



(legend on next page)

Retrogradely traced cell bodies were visualized in the nodose ganglion (Figure 1C). Centrally, TdTomato-expressing fibers were present through the caudal portion of the nucleus of the solitary tract (NTS) and the area postrema (AP) (Figure 1D), an indication that pseudounipolar nodose ganglion neurons directly connect the LV to the dorsal vagal complex—a main integrative relay station that processes interoceptive information to command adaptive efferent responses.³¹ To verify the selectivity of virus injections in the heart, we controlled for potential viral spread to other tissues analyzing the reporter expression in the liver, a non-relevant organ. No TdTomato signal was present, indicating specificity of intracardiac injections (Figure S4A).

To investigate the functional relevance of neurons integrating the vagal afferents, we analyzed FOS expression—a robust marker of neuronal activation—in the dorsal vagal complex of mice subjected to TAC for 1 day accompanied by sham controls. We found significantly increased FOS expression in the NTS and dorsal motor nucleus of the vagus nerve (DMV) of TAC mice, suggesting an early recruitment of these structures in response to LV pressure overload (Figures 1E and 1F).

Pressure overload recruits a vagus nerve-mediated brain-to-spleen circuit

The vagus nerve modulates splenic immunity through a celiac efferent arm that directly connects to the sympathetic splenic nerve in the celiac ganglion and induces neurotransmitter release in the spleen.^{24,25,32–34} To examine the neuronal activity of components constituting the heart-brain-spleen axis, we recorded nerve firing and found elevation of celiac vagus nerve activity (CVNA) (Figure 1G) and splenic sympathetic nerve activity (SSNA) 1 day after TAC (Figure 1H). Celiac vagus denervation significantly reduced the SSNA increased by TAC (Figures S4B and S4C), indicating a dependence of the TAC-induced splenic nerve activation on the vagal reflex. Together, this evidence suggests that cardiac vagal afferents signal to neurons in the dorsal vagal complex to increase the efferent vagus nerve activity and sympathetic outflow to the spleen.

To investigate the relevance of this neural circuit in HTN-HD, we performed a celiac ganglionectomy (CGX), hence denervating the spleen, in mice concomitantly subjected to TAC or sham procedure (Figure S4D). CGX was effective in reducing tyrosine hydroxylase (TH)—the rate-limiting enzyme of norepinephrine synthesis—in the splenic marginal zone delimited by

CD169⁺ metallophilic macrophages (Figure S4E). No effect of CGX was observed on cardiac morphology and function, as well as on the immune profile, in basal conditions. However, CGX hampered TAC-induced cardiac macrophages' expansion (Figures 1I and 1J) and adaptive hypertrophic remodeling, as shown by the reduced ejection fraction (EF) and RWT of denervated mice (Figures 1L and 1M; Table S1). To examine whether the neural reflex was required at the establishment of the LV response to pressure overload or overtime, we denervated mice by CGX in the second week after TAC (Figure S4F), when the adaptive remodeling was already established. In this case, CGX, while similarly showing effective denervation of the spleen (Figure S4G), did not affect the adaptive cardiac remodeling to pressure overload (Figures S4H and S4I), indicating that the neural reflex converging on the spleen is indispensable at the onset of cardiac remodeling but not during its progression.

The SNS has also been implicated in LV hypertrophy to pressure overload through increased cardiac sympathetic activity,²¹ and SNS efferent fibers originating from the cervical ganglion (CerG) modulate cardiac innate immunity during myocardial infarction.³⁵ Here, we examined the role of local SNS in cardiac remodeling and immune cells activation during TAC. The surgical removal of the CerG (CerGX) abrogated LV sympathetic innervation (Figures S5A–S5C) but had no effect on the cardiac macrophages either in basal conditions or 4 days after TAC-induced pressure overload (Figures 1I and 1K). Similarly, CerGX did not alter basal cardiac function and structure and the process of LV hypertrophic remodeling to pressure overload (Figures 1N and 1O; Table S1). Since both CGX and CerGX abrogate sympathetic innervation, we wanted to exclude that they could influence the degree of pressure overload imposed on the LV through the aortic coarctation. Neither CGX nor CerGX had any effect on hemodynamic parameters evaluated by measuring the *trans* stenotic gradient through Doppler analysis and systolic blood pressure in the carotid arteries upstream to the ligation (Figures S5D and S5E). Collectively, these results reveal that the sympathetic nerve input to distant organ (the spleen) is essential for LV adaptation to TAC, while local sympathetic nerve input (to the heart) is dispensable.

The spleen protects from HTN-HD development

Since the spleen constitutes a reservoir of immune cells that can be promptly deployed upon emergency conditions, we explored

Figure 2. Spleen is necessary for LV adaptation to pressure overload, independently from monocyte-derived macrophages

(A) LV M-mode echocardiography 8 weeks after TAC in splenectomized mice (–spleen) or control with intact spleen (+spleen). (B and C) Serial LV echocardiography in basal condition and 1–2–4–8 weeks after TAC in mice –spleen or +spleen. EF (B) and RWT (C) are shown. $n = 3$ sham +spleen; $n = 4$ TAC +spleen; $n = 8$ sham –spleen; $n = 8$ TAC –spleen. Data as mean \pm SEM and analyzed by two-way ANOVA and Tukey post hoc. \$\$\$ $p < 0.001$ sham +spleen vs. TAC +spleen; ### $p < 0.001$ sham –spleen vs. TAC –spleen; * $p < 0.05$, *** $p < 0.001$ TAC +spleen vs. TAC –spleen. (D–G) Flow cytometry (D) and quantification of total CD11b⁺CD64⁺ Mac (E), Timd4[–]Ly6C^{lo} RMs (F), and Timd4[–]Ly6C^{hi} recruited Mac (G) in the LV of TAC –spleen or TAC +spleen mice. $n = 4$ sham +spleen; $n = 5$ TAC +spleen; $n = 5$ sham –spleen; $n = 5$ TAC –spleen. Data as mean \pm SEM and analyzed by two-way ANOVA and Tukey post hoc. * $p < 0.05$, ** $p < 0.01$, *** $p < 0.001$. (H–K) Flow cytometry (H) and quantification of total CD11b⁺CD64⁺ Mac (I), Timd4[–]Ly6C^{lo} RMs (J), and Timd4[–]Ly6C^{hi} recruited Mac (K) in the LV of *Nr4a1*^{–/–} and WT mice after TAC or sham. $n = 3$ WT sham; $n = 6$ WT TAC; $n = 3$ *Nr4a1*^{–/–} sham; $n = 6$ *Nr4a1*^{–/–} TAC. Data as mean \pm SEM and analyzed by two-way ANOVA and Tukey post hoc. * $p < 0.05$, ** $p < 0.01$. (L) Flow cytometry quantification of circulating Ly6C^{lo} monocytes in *Nr4a1*^{–/–} and WT mice after TAC or sham. $n = 3$ WT sham; $n = 4$ WT TAC; $n = 3$ *Nr4a1*^{–/–} sham; $n = 6$ *Nr4a1*^{–/–} TAC. Data as mean \pm SEM and analyzed by two-way ANOVA and Tukey post hoc. * $p < 0.05$, ** $p < 0.01$. (M–P) Serial LV echocardiography in basal condition and 1–2–4–8 weeks after TAC in *Nr4a1*^{–/–} and WT mice (M and N) and in *Ccr2*^{–/–} and WT mice (O and P). EF and RWT are shown. $n = 8$ WT TAC; $n = 5$ *Nr4a1*^{–/–} TAC. $n = 5$ WT TAC; $n = 5$ *Ccr2*^{–/–} TAC. Data as mean \pm SEM and analyzed by two-way ANOVA and Sidak post hoc. Schematics were created with BioRender.com. See also Tables S2 and S3.

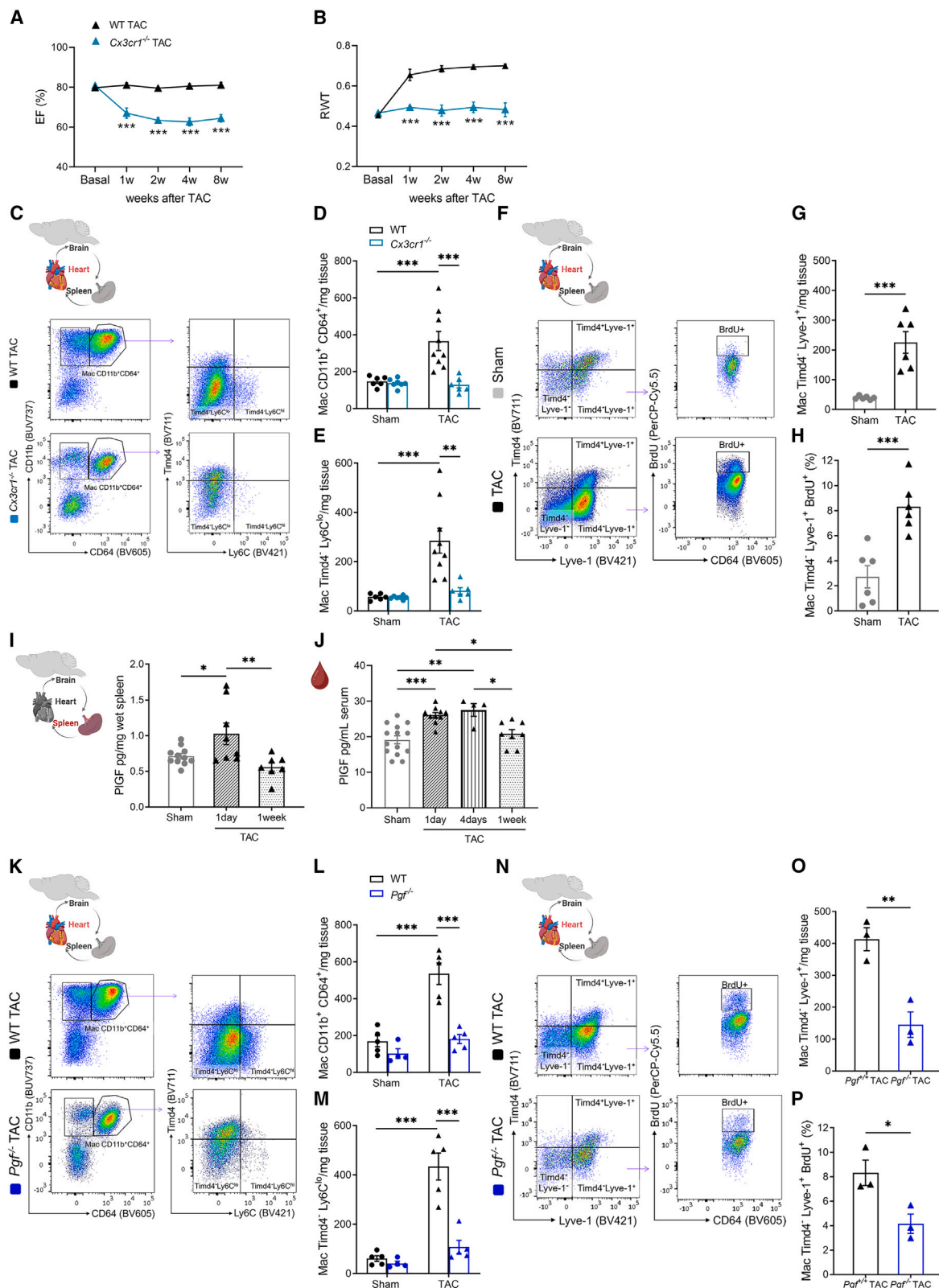


Figure 3. TAC stimulates splenic PIGF secretion to induce cardiac RM proliferation and counteract HF

(A and B) Serial LV echocardiography in basal condition and 1–2–4–8 weeks after TAC in *Cx3cr1*^{-/-} and WT mice. EF (A) and RWT (B) are shown. *n* = 4 WT TAC; *n* = 5 *Cx3cr1*^{-/-} TAC. Data as mean ± SEM and analyzed by two-way ANOVA and Sidak post hoc. ****p* < 0.001.

(legend continued on next page)

the potential dependence of TAC-induced cardiac macrophage expansion on recruited monocytes.¹⁷

We performed sham or TAC in mice previously subjected to splenectomy or to the respective control procedure and analyzed cardiac remodeling. While splenectomy per se had no effect on cardiac structure and immune profile, splenectomized mice developed HF after TAC, presenting LV dilation and absence of LV adaptive hypertrophy (Figures 2A–2C; Table S2). Flow cytometry revealed a failure in expanding both resident and recently recruited cardiac macrophages early after TAC (Figures 2D–2G), indicating that the spleen has a necessary and non-redundant role in promoting LV macrophage expansion and adaptive remodeling to pressure overload.

The recruitment of Ly6C^{hi} monocytes leads to the development of CD11b⁺CD64⁺ Ly6C^{lo} cells through the orphan nuclear hormone receptor—nuclear receptor subfamily 4 group a member 1 (NR4a1)—and subsequent maturation into tissue macrophages.³⁶ We addressed the potential involvement of this pathway by using *Nr4a1*^{−/−} mice. Flow cytometry indicated a significant expansion of cardiac macrophages in the LV of *Nr4a1*^{−/−} mice subjected to pressure overload, to an extent comparable to WT (Figures 2H–2K), while, as expected, the inhibition of this pathway selectively impaired the Ly6C^{lo} fraction of circulating monocytes (Figure 2L). The absence of NR4a1 did not influence the evolution of cardiac remodeling to pressure overload that was comparable to that of WT mice (Figures 2M and 2N; Table S3). More in detail, *Nr4a1*^{−/−} mice subjected to TAC established an adaptive hypertrophic remodeling, characterized by long-term preservation of EF (Figure 2M). A similar LVPW;d thickening was reached in the two groups of mice and was accompanied by a comparable LVID;d reduction (Table S3). This effect was reflected by overlapping RWT values displayed over time by *Nr4a1*^{−/−} and WT mice (Figure 2N). Hence, Ly6C^{hi} monocytes recruited into the LV in response to TAC and transitioning into Ly6C^{lo} macrophages through NR4a1 did not contribute to the macrophage expansion required to withstand pressure-induced cardiac stress. To further support this conclusion and exclude the involvement of Ly6C^{hi} monocyte-derived macrophages through other mechanisms, we took advantage of *Ccr2*^{−/−} mice, which lack the receptor necessary to recruit Ly6C^{hi} monocytes into inflamed tissues. We found that *Ccr2*^{−/−} mice established LV adaptive hypertrophy with EF preserved over time (Figures 2O and 2P; Table S3). Collectively, the above results led us to hypothesize that the spleen

contributes to LV macrophage expansion through other mechanisms, possibly depending on soluble mediators with paracrine functions.

RMs proliferate in response to cardiac stress and are necessary to hamper HF

RMs express CX(3)-C-motif chemokine receptor-1 (*Cx3cr1*)—the high-affinity functional chemokine receptor for fractalkine (CX3CL1).¹⁶ Hence, it is possible to assess their role in cardiac remodeling by subjecting mice lacking this receptor to pressure overload. *Cx3cr1*^{−/−} mice did not establish adaptive hypertrophy upon TAC, progressing toward LV dilation and early decline of EF (Figures 3A and 3B; Table S4). Analysis of the immune response showed no differences in cardiac macrophage populations between *Cx3cr1*^{−/−} and WT mice at baseline (Figures 3C–3E). After TAC, *Cx3cr1*^{−/−} mice had an impaired expansion of total cardiac macrophages, particularly of the Tmd4⁺Ly6C^{lo} subpopulation (Figures 3C–3E), indicating that cardiac RMs are essential for LV adaptation to pressure overload.

Besides replenishment by recently recruited cells, cardiac macrophages expand through *in situ* proliferation.^{16,17} To analyze the proliferation of cardiac RMs, we further characterized the Tmd4⁺Ly6C^{lo} macrophages by the expression of another marker of tissue residency, the lymphatic vessel endothelial hyaluronan receptor 1 (Lyve-1) (Figure S6A). To determine macrophages' replicative potential, mice were administered bromodeoxyuridine (BrdU) before heart harvest and flow cytometry (Figure S6B). TAC induced a numerical expansion of LV Ly6C^{lo}Tmd4⁺Lyve-1⁺ macrophages (Figures 3F and 3G), which showed a significant proliferative burst as compared with sham (Figures 3F, 3H, S6A, and S6C for the gating strategy). These data indicate that pressure overload induces local proliferation in cardiac RMs, contributing to LV adaptation to hemodynamic overload.

SNS-mediated PIGF release connects the spleen to the pressure-overloaded heart

We previously found that *Pgfr*^{−/−} mice develop unfavorable remodeling to pressure overload.¹⁴ Also, we have shown that other hypertensive stimuli, like angiotensin II, promote splenic secretion of PIGF in response to the cholinergic-sympathetic pathway.²⁴ Here, we analyzed PIGF secretion in response to pressure overload. TAC induced a significant and rapid increase in PIGF expression in the spleen that returned to the steady state

(C–E) Flow cytometry (C) and quantification of total CD11b⁺CD64⁺ Mac (D) and Tmd4⁺Ly6C^{lo} RMs (E) in the LV of *Cx3cr1*^{−/−} and WT mice after TAC or sham. *n* = 6 WT sham; *n* = 9 WT TAC; *n* = 7 *Cx3cr1*^{−/−} sham; *n* = 6 *Cx3cr1*^{−/−} TAC. Data as mean ± SEM and analyzed by two-way ANOVA and Tukey post hoc. ***p* < 0.01, ****p* < 0.001.

(F–H) Flow cytometry analysis (F) and quantification of cardiac Ly6C^{lo}Tmd4⁺ RM expressing Lyve-1 (G), and relative BrdU incorporation (H) after TAC or sham. *n* = 6 sham; *n* = 7 TAC. Data as mean ± SEM and analyzed by unpaired t test, ***p* < 0.01, ****p* < 0.001.

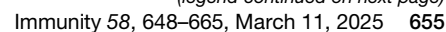
(I) Splenic PIGF in 1-day TAC, 1-week TAC, or sham mice. *n* = 11 sham; *n* = 8 TAC 1 day; *n* = 7 TAC 1 week. Data as mean ± SEM and analyzed by one-way ANOVA and Tukey post hoc. **p* < 0.05, ***p* < 0.01.

(J) Circulating PIGF in 1-day TAC, 4-day TAC, and 1-week TAC or sham mice. *n* = 14 sham; *n* = 10 TAC 1 day; *n* = 4 TAC 4 days; *n* = 8 TAC 1 week. Data as mean ± SEM and analyzed by one-way ANOVA and Tukey post hoc. **p* < 0.05, ***p* < 0.01, ****p* < 0.001.

(K–M) Flow cytometry (K) and quantification of LV CD11b⁺CD64⁺ Mac (L) and Tmd4⁺Ly6C^{lo} RMs (M) in LV of *Pgfr*^{−/−} and WT mice 4 days after TAC or sham. *n* = 5 WT sham; *n* = 5 WT TAC; *n* = 4 *Pgfr*^{−/−} sham; *n* = 5 *Pgfr*^{−/−} TAC. Data as mean ± SEM and analyzed by two-way ANOVA and Tukey post hoc. ****p* < 0.001.

(N–P) Flow cytometry (N) and quantification of cardiac Ly6C^{lo}Tmd4⁺Lyve-1⁺ RMs (O) and relative BrdU incorporation (P) in *Pgfr*^{−/−} and WT mice 4 days after TAC or sham. *n* = 3 WT TAC; *n* = 3 *Pgfr*^{−/−} TAC. Data as mean ± SEM and analyzed by unpaired t test. **p* < 0.05, ***p* < 0.01. Schematics were created with BioRender.com.

See also Figure S6 and Table S4.



at 1 week after TAC (Figure 3I). Circulating amounts of PIGF increased 1 day after TAC, continued to rise, reaching a plateau at 4 days after TAC, and returned to the baseline 1 week after TAC, when the adaptive cardiac remodeling was well established (Figure 3J). Hence, we analyzed the cardiac immune response to TAC in *Pgfr*^{-/-} mice, which failed to expand cardiac macrophages (Figures 3K and 3L) and, particularly, the fraction of Timd4⁺Ly6C^{lo} RMs, which remained comparable to that of sham-operated mice (Figures 3K and 3M). In addition, the proliferation of Ly6C^{lo}Timd4⁺Lyve-1⁺ RMs, which was responsible for their numerical expansion during TAC, was significantly impaired in the absence of PIGF (Figures 3N–3P).

Pressure overload induced PIGF secretion in the marginal zone of the spleen, delimited by ERTR7⁺ fibroblast reticular cells (Figures 4A and 4B), where TH-positive fibers sprout from the splenic nerve.^{24,32} To test the dependence of splenic PIGF increase on TAC-induced cholinergic-sympathetic outflow, we denervated mice through CGX. As shown in Figures 4A and 4B, TAC failed to increase PIGF secretion in the spleen of denervated mice. Also, CGX mice subjected to TAC did not elevate PIGF amounts in the circulation, remaining similar to that of control mice (Figure S6D). Then, we analyzed the proliferation of cardiac macrophages induced by TAC in splenectomized mice or in mice subjected to CGX. When we removed the spleen or its sympathetic innervation, cardiac Ly6C^{lo}Timd4⁺Lyve-1⁺ RMs did not proliferate in response to TAC (Figures 4C–4E). These data suggest that the celiac vagus reflex mediated splenic PIGF secretion and influenced cardiac macrophages' proliferation, which in turn contributed to adaptive cardiac remodeling.

To prove the mechanistic role of splenic PIGF, we generated chimeric mice by spleen transplantation between *Pgfr*^{-/-} and WT mice and subjected them to TAC (Figure 4F). Splenic-deficient PIGF mice (*Pgfr*^{-/-} spleen in WT mice) were unable to counteract TAC-induced pressure overload, displaying an absence of LV adaptive remodeling and a decline of EF and LV dilation (Figures 4G–4I; Table S5), thus phenocopying the response of PIGF-deficient mice.¹⁴ Conversely, it was sufficient to reconstitute splenic PIGF by transplanting WT spleens in PIGF-deficient mice (WT spleen in *Pgfr*^{-/-} mice) to hamper HF (Figures 4G–4I; Table S5). A similar result was obtained by administering recombinant PIGF (rPIGF) to splenectomized mice, which normally develop HF when subjected to TAC. The treatment with rPIGF rescued splenectomized mice from HF development (Figures 4J and 4K; Table S5), indicating the capability of PIGF to exert a cytokine-like effect at a distant site (the heart).

NRP1 identifies cardiac macrophages essential for adaptive hypertrophy during hypertensive stress

A recent single-cell RNA sequencing (scRNA-seq) study has characterized the multitude of macrophage clusters present in the heart of mice subjected to TAC during the compensatory hypertrophic phase or sham as control.¹⁹ Cardiac macrophages showed an upregulation of *Nrp1* gene, which encodes the transmembrane glycoprotein acting as a PIGF receptor.^{37,38} To investigate *Nrp1* expression, we re-analyzed publicly available data by Revelo and colleagues¹⁹ of sorted immune cells from sham and TAC mice. We annotated each cell type based on canonical makers (Figures 5A and 5B) and analyzed expression of *Nrp1* in various cell types. Macrophages had the highest expression of *Nrp1* compared with other immune cells (Figures 5C and 5D). However, we observed no significant transcriptional changes with TAC. We extracted and re-clustered macrophages into the heterogeneous subsets based on expression of *Timd4*, *Lyve-1*, and *Ccr2* markers,^{16,39} finding that self-renewing RM expressing *Timd4* and *Lyve-1* had the highest expression of *Nrp1* mRNA while CCR2⁺ recruited macrophages had the least expression (Figures 5E–5G). These results indicated that the resident population, but not the recruited one, might be responsive to PIGF. Also, there was no statistically significant difference in *Nrp1* mRNA expression between sham and TAC, suggesting a post-transcriptional regulation of NRP1. To validate this hypothesis, we used the flow cytometry gating strategy in Figure S7A to identify NRP1⁺ cardiac macrophages. TAC significantly increased NRP1 expression on cardiac Ly6C^{lo}Timd4⁺Lyve-1⁺ RMs (Figures 6A and 6B), but not in other macrophage subpopulations (Figures S7B and S7C), suggesting that the effect of PIGF was selective on those macrophages.

To examine the role of NRP1 in HTN-HD, we generated an NRP1 myeloid-specific-deficient model by crossing *Nrp1*-floxed (*Nrp1*^{fl/fl}) with *Lyz2*-cre mice, obtaining the *Nrp1*^{fl/fl}; *Lyz2*-cre progeny. *Nrp1*^{fl/fl}; *Lyz2*^{cre/+} mice showed lower amounts of NRP1 in cardiac macrophages (Figures S7A and S7B). The lack of NRP1 did not affect LV macrophage populations at the steady state (Figures 6C–6E). However, it significantly hampered the TAC-induced expansion of Timd4⁺Ly6C^{lo} RMs (Figures 6C–6E) and the proliferation rate of the Lyve-1⁺ subset (Figures 6F–6H). More importantly, *Nrp1*^{fl/fl}; *Lyz2*^{cre/+} mice subjected to TAC developed HF characterized by an impairment of the LV adaptive hypertrophy (Figures 6I and 6J; Table S6). While we found that both resident and partially replenished macrophages expanded during TAC, our data suggest a selective effect of PIGF on the subset independent from recruited monocytes. Hence, we generated another model to selectively target the resident

(C–E) Flow cytometry (C) and quantification of cardiac Ly6C^{lo}Timd4⁺Lyve-1⁺ RMs (D) and relative BrdU incorporation (E) in mice subjected to TAC for 4 days and to splenectomy or CGX, and in relative controls. *n* = 5 TAC; *n* = 3 TAC –spleen; *n* = 3 TAC CGX. Data as mean ± SEM and analyzed by one-way ANOVA and Tukey post hoc. **p* < 0.05, ***p* < 0.01, ****p* < 0.001.

(F) Schematics of spleen transplantation between *Pgfr*^{-/-} and WT mice.

(G) LV M-mode echocardiography 5 weeks after TAC in mice subjected to spleen transplantation.

(H and I) LV echocardiography in basal condition and at the endpoint after TAC in WT mice with *Pgfr*^{-/-} spleen or *Pgfr*^{-/-} mice with WT spleen. EF (H) and RWT (I) are shown. *n* = 4 WT mice with *Pgfr*^{-/-} spleen; *n* = 3 *Pgfr*^{-/-} mice with WT spleen. Data as mean ± SEM and analyzed by two-way ANOVA and Sidak post hoc. ***p* < 0.01, ****p* < 0.001.

(J and K) LV echocardiography in basal condition and at the endpoint after TAC in splenectomized mice (–spleen) treated with rPIGF or vehicle. EF (J) and RWT (K) are shown. *n* = 5 TAC –spleen veh; *n* = 4 TAC –spleen rPIGF. Data as mean ± SEM and analyzed by two-way ANOVA and Sidak post hoc. **p* < 0.05, ***p* < 0.01. Schematics were created with BioRender.com.

See also Figure S6 and Table S5.

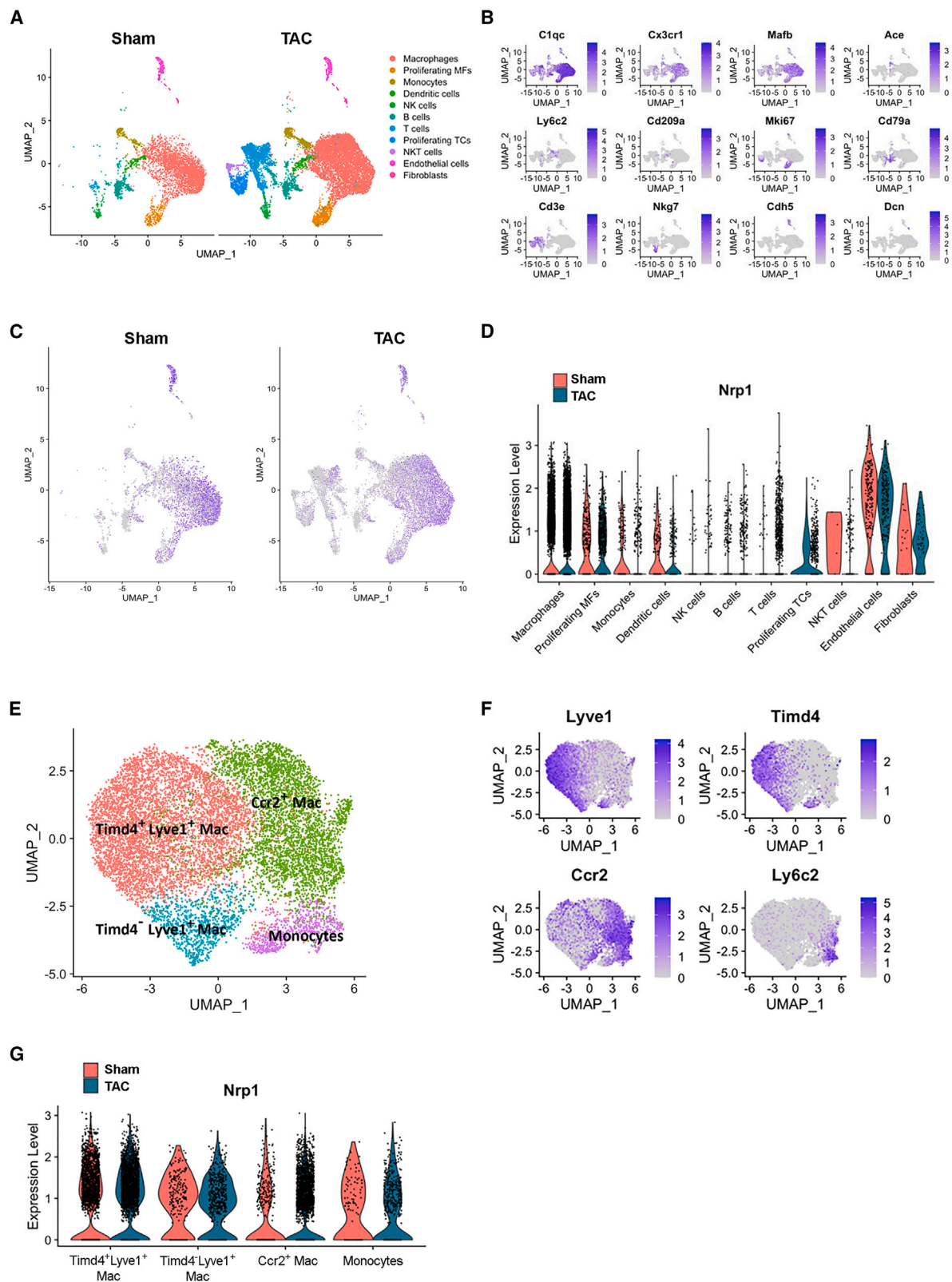


Figure 5. scRNA-seq of cardiac immune cells shows a cluster of NRP1^+ RMs

(A) Uniform manifold approximation and projection (UMAP) of single cells clustered in 11 unique clusters. Sham and TAC-derived cells are plotted separately to visualize abundance differences.

pool of macrophages. We crossbred the *Rosa26*^{LSL-RFP/+}; *Cx3cr1*^{Cre-ERT2/+} (RM^{RFP}) cre recombinase mouse model with *Nrp1*^{fl/fl} mice and obtained *Nrp1*^{fl/fl}; *Rosa26*^{LSL-RFP/+}; *Cx3cr1*^{Cre-ERT2/+} (RM^{RFP-ΔNrp1}), which lacks NRP1 in RMs but not in recruited cells (Figure S7D). RM^{RFP-ΔNrp1} mice subjected to TAC showed maladaptive cardiac remodeling with early reduction of EF and decreased RWT (Figures 6K and 6L; Table S6). Subsequently, we evaluated the BrdU+ macrophages in the LV of RM^{RFP-ΔNrp1} and RM^{RFP} mice 4 days after TAC, finding that, in the absence of NRP1, resident RFP+ macrophages did not expand by local proliferation (Figures 6M, 6N, and S7D).

Neural-mediated PIGF-NRP1 signaling in profibrotic cardiac RMs promotes adaptive hypertrophy

To investigate how PIGF-NRP1 signaling affects RM functions with beneficial effects on cardiac remodeling to TAC, we analyzed insulin-like growth factor-1 (IGF-1), previously shown as a key adaptive growth factor produced by RMs in the stressed LV.^{18,27} 4 days of TAC increased amounts of IGF-1 in cardiac homogenates of WT mice (Figure 7A). On the contrary, mice with an impairment of PIGF-NRP1 pathway, obtained by *Nrp1*^{fl/fl}; *Lyz2*^{cre/+} or *Pgf*^{-/-}, did not increase IGF-1, which remained similar to sham controls (Figure 7A). This finding suggested that PIGF-NRP1 signaling induced an adaptive hypertrophic response through IGF-1.

Adaptive hypertrophy is also often associated with the apposition of fibrosis by interstitial collagen accumulation,⁴⁰ which might be regulated by specific profibrotic RMs. Here, we found that TAC induced a significant surge of the total abundance of CD206⁺ profibrotic macrophages (Figures 7B and 7C), which was abolished in mice lacking PIGF or its receptor NRP1 in myeloid cells (Figures 7B and 7C). We further tested whether NRP1 expression on the RM expanding during TAC characterizes the profibrotic subset. By analyzing the fraction of Ly6C^{lo}Timd4⁻Lyve-1⁺Nrp1⁺ RM expressing CD206, we found that its abundance was significantly reduced in mice lacking PIGF and, as expected, completely absent in *Nrp1*^{fl/fl}; *Lyz2*^{cre/+} mice (Figure 7D). In addition, we analyzed the same pools of macrophages in mice that do not have spleen or its innervation to test the dependence on the celiac vagus reflex. We found that CD206⁺ RMs did not expand in both conditions (Figures 7E–7G), suggesting that the loss of phagocytic and profibrotic macrophages could impair the process of adaptive collagen deposition when the heart-brain-spleen axis is blocked. To explore this issue, we analyzed the content of interstitial fibrosis in splenectomized or CGX mice subjected to TAC by quantifying the thick collagen bands in the LV at the end point of the remodeling process. All the collagen deposition observed in TAC LV appeared as thick bands of interstitial fibrosis, usually associated with cardiomyocyte growth to sustain the myocardium to withstand pressure-induced stress. Notably, mice lack-

ing the spleen (–spleen) or the celiac ganglion innervation did not show interstitial fibrosis (Figures 7H and 7I), while manifesting maladaptive cardiac remodeling and HF. These data suggest that the neuroimmune-mediated release of PIGF regulates the profibrotic fraction of cardiac RM expressing NRP1, which might mediate the apposition of interstitial collagen in the overloaded heart necessary to sustain cardiac function.

PIGF correlates with hypertension, and NRP1+ RMs are conserved in human HF

To explore the involvement of PIGF-NRP1 pathway in human HTN-HD, we assessed the amounts of circulating PIGF in a cohort of patients with a history of hypertension. Hypertensive patients and normotensive controls were stratified according to parameters of cardiac remodeling obtained by echocardiographic analysis. We considered both LV mass increase and LV wall/LV diameter ratio and performed a tertiles split achieved on a compound score obtained by the sum of min-max normalized RWT and LV mass index (LVMI). Patients in the lower tertile were hypertensive, showing no hypertrophic remodeling, and were grouped with normotensive. Patients in the second and third tertiles showed either increased RWT or LVMI or both. This latter group was characterized by increased amounts of circulating PIGF that accompanied the hypertrophic cardiac remodeling (Figure 7J). Furthermore, we evaluated the gene expression of NRP1 in the myocardial tissue collected from cardiac biopsies from HF patients, observing a positive correlation between NRP1 amounts and the expression of the macrophage marker CD68 (Figure 7K; Table S7). To further validate these data, we analyzed NRP1 expression in tissue macrophages. By CCR2 expression, we discriminated between the fraction of macrophages replenished by recruited monocytes (CD68⁺CCR2⁺) and the fraction of RMs (CD68⁺CCR2⁻), finding that NRP1 was predominantly expressed by cardiac CD68⁺CCR2⁻ RMs (Figures 7L and 7M). Our results demonstrate that the PIGF-NRP1 pathway is conserved in human HTN-HD.

DISCUSSION

In this work, we demonstrated that cardiac architectural adaptations capable of withstanding the LV pressure overload imposed by hypertension necessitate a heart-brain-spleen axis. This brain-body communication activates cardiac RMs that, in turn, allow the myocardium to execute the morphological adjustments required to sustain LV function. In particular, we showed that cardiac pressure overload activated a neural circuit converging on the spleen through the cholinergic-sympathetic pathway. The release of PIGF evoked by vagus-splenic neural activity promoted adaptive remodeling by modulating cardiac RM expressing its cognate receptor NRP1. In patients with hypertension, we showed that circulating amounts of PIGF were increased and correlated with cardiac hypertrophic remodeling. In addition,

(B) Feature plots depicting the single-cell expression of key cluster-defining genes.

(C) Feature plot depicting *Nrp1* expression in TAC vs. sham cells.

(D) Violin plot of *Nrp1* expression in each cluster.

(E) UMAP of macrophages and monocytes re-clustered separately to reveal increased heterogeneity.

(F) Feature plots of key resident vs. recruited macrophage genes.

(G) Violin plot of *Nrp1* expression for each macrophage cluster in sham vs. TAC conditions.

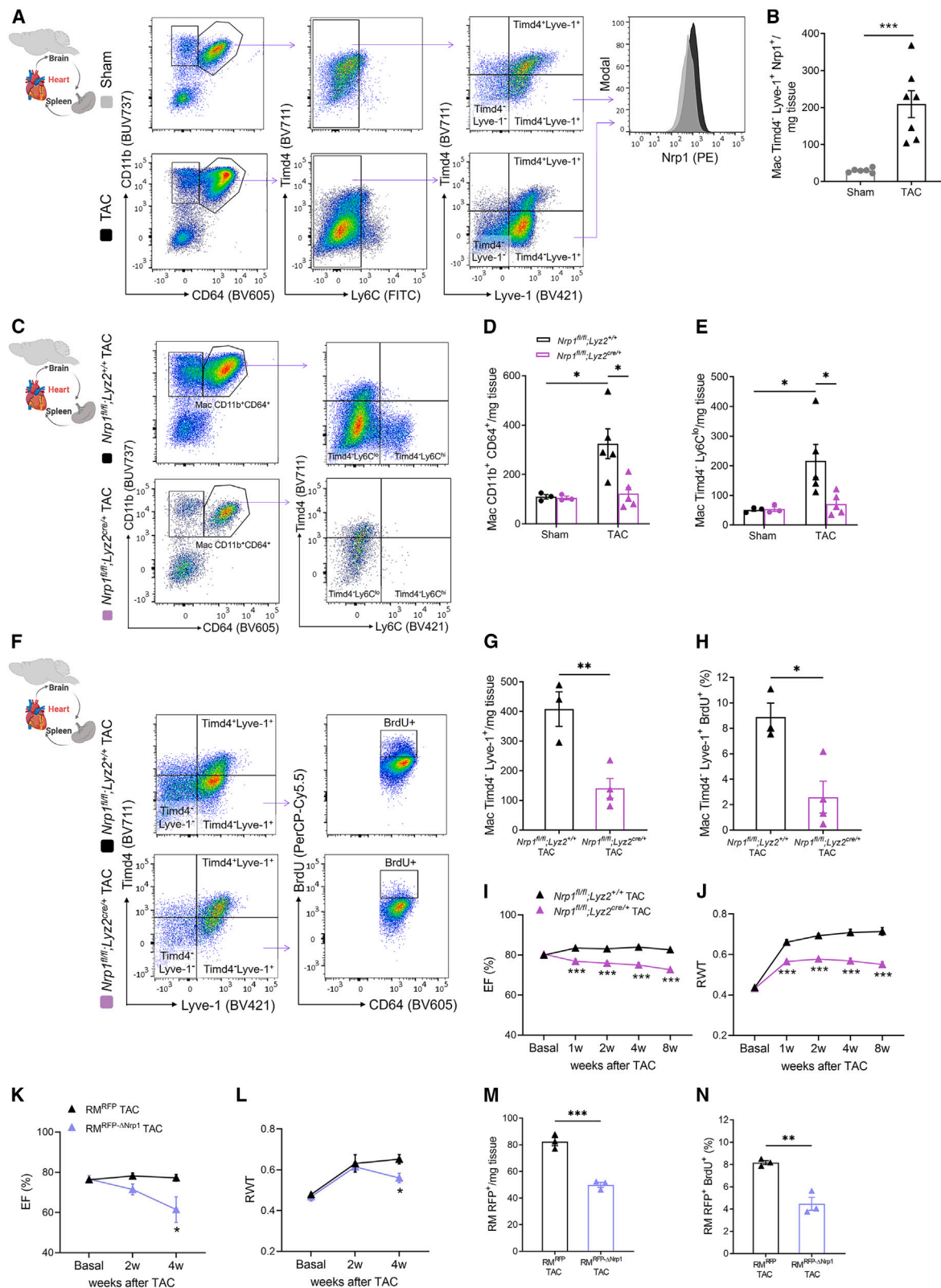


Figure 6. PIGF-NRP1 mediates adaptive functions of macrophages during pressure overload

(A and B) Flow cytometry (A) and quantification (B) of NRP1 expression in cardiac Ly6C⁺Timd4⁺Lyve-1⁺ RMs after TAC. *n* = 6 sham; *n* = 7 TAC. Data as mean ± SEM and analyzed by unpaired t test. ****p* < 0.001.

(legend continued on next page)

NRP1 was expressed by cardiac RMs, analyzed in a subset of available cardiac biopsies.

We observed that early adaptive cardiac remodeling is associated with a significant numerical increase of macrophages. These results imply the existence of a crosstalk between the immune system and heart and indicate that TAC recruits a multi-organ response to establish an adaptive cardiac remodeling that hampers HF progression. The ANS represents one of the master regulators of our body's integrative systems. We discovered that a specific ANS efferent pathway, mediated by the celiac vagus and the splenic sympathetic nerves, is involved in hypertension^{24,25,33,41} and atherosclerosis.³⁹ Here, we have shown that the heart established a direct connection with the brain dorsal vagal complex, whereby the ultrasound-guided injection of AAV2/retro-CAG-TdTomato virus in LV walls identified a circuit connecting the heart to the pseudounipolar neurons of the nodose ganglion back to the brainstem, whose neurons were activated by TAC. A subsequent surge in the CVNA and SSNA firing with consequent TH-mediated neurotransmitter release in the spleen established the efferent reflex. Mice subjected to a selective denervation of this pathway developed maladaptive cardiac remodeling to hypertensive stress, accompanied by impaired expansion of macrophages. Since pressure overload induces a generalized increase in sympathetic activity, we questioned whether enhanced SNS activity in other districts, particularly the local one acting on the LV, could be relevant for cardiac remodeling. On this note, it has been shown that impairment of direct cardiac innervation obtained by CerGX removal³⁵ or during aging⁴² induces cardiac dysfunction. On the other hand, it was found that the superior cervical ganglia respond to pressure overload with macrophages' accumulation, fibrosis, and deterioration of neurons innervating the pineal gland,⁴³ with consequences on the sleep-wake pattern but not on cardiac disease itself. Here, when we selectively denervated the heart by CerGX removal, no perturbation of cardiac macrophages' expansion and LV adaptation was observed in response to pressure overload. Hence, these results highlight the necessary and non-redundant role of sympathetic nerve input to a distant organ—the spleen—for LV adaptation to TAC.

The observation that macrophages expanded upon TAC and that innervation of a distant organ like the spleen is indispensable led us to hypothesize a potential contribution of monocyte-derived macrophages of splenic origin in adaptive cardiac remodeling. Notably, macrophages did not expand in splenectomized mice subjected to pressure overload, which displayed early HF. However, by subsequently utilizing *Ccr2*^{-/-} and *Nr4a1*^{-/-}

mice, we excluded a role for CD11b⁺CD64⁺Ly6C^{hi} monocytes, which are recruited through CCR2 and locally differentiate into macrophages through NR4a1. These findings led to evaluating the proliferation potential of resident cells, which in fact significantly incorporated BrdU administered before heart harvest. Taken together, these results suggest that proliferation and not replenishment is responsible for the expansion of macrophages that contribute to LV adaptive remodeling during TAC.

We have previously demonstrated that the spleen is a reservoir of PIGF in hypertension.^{24,33} In this study, we showed that TAC induced a noradrenergic-dependent rapid secretion of PIGF in the splenic marginal zone, with subsequent release in the circulation to exert paracrine effects in the heart. This concept was supported by three findings. First, mice lacking PIGF and subjected to TAC did not expand cardiac RMs and develop HF.¹⁴ Second, transplantation of a WT spleen into PIGF-deficient mice rescued the phenotype. Third, similarly, the administration of rPIGF to splenectomized mice, which similarly develop HF, rescued the maladaptive cardiac phenotype. Notably, another study identified a heart-brain-kidney inter-organ crosstalk involved in cardiac remodeling to pressure overload.²⁸ While this work did not analyze the brain areas involved in the process, the authors proposed that pressure overload enhances renal sympathetic activity, leading to the secretion of colony-stimulating factor 2 (CSF2) cytokine to activate cardioprotective functions of RMs.²⁸

In our study, we further investigated how a cardioprotective factor produced by a distant organ handles cardiac macrophages during pressure overload. Mining the data obtained by a recent work that screened the differential gene expression of cardiac macrophage clusters in the heart subjected to TAC,¹⁹ we observed that the PIGF receptor, NRP1, characterizes a specific cluster of cardiac RMs. We observed a significant increase of NRP1 expression in cardiac RMs that proliferated during pressure overload, and its selective genetic ablation in macrophages hampered the myocardium's ability to preserve cardiac function. It has been previously shown that cardiac RMs orchestrate adaptive hypertrophic remodeling during hypertensive stress by producing IGF-1.²⁷ Here, we found that IGF-1-mediated cardioprotective mechanism depends on PIGF-NRP1 signaling in cardiac macrophages, as pressure overload increases IGF-1 in the heart of WT mice but not of *Nrp1*^{fl/fl}; *Ly22*^{cre/+} and *Pgf*^{-/-} mice. Our work demonstrates how local cardiac mediators—like IGF-1—can be affected by distant organs like the spleen through a neural-mediated reflex.

In the complexity of mechanisms contributing to cardiac remodeling in response to pressure overload, fibrosis might be a

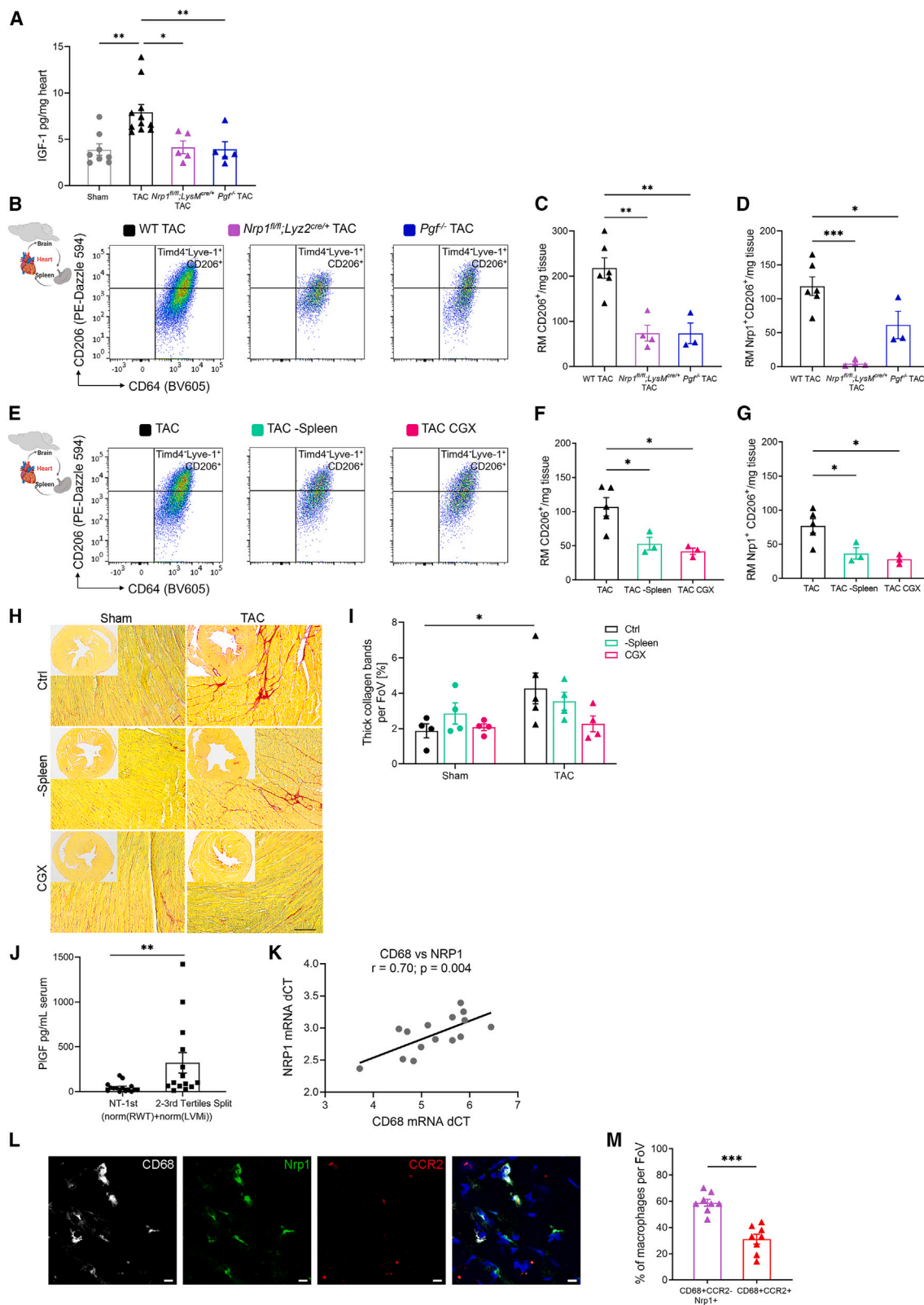
(C–E) Flow cytometry (C) and quantification of total CD11b⁺CD64⁺ Mac (D) and Timd4⁺Ly6C^{lo} RMs (E) in the LV of *Nrp1*^{fl/fl}; *Ly22*^{cre/+} and *Nrp1*^{fl/fl}; *Ly22*^{+/+} mice after TAC or sham. *n* = 3 *Nrp1*^{fl/fl}; *Ly22*^{+/+} sham; *n* = 5 *Nrp1*^{fl/fl}; *Ly22*^{+/+} TAC; *n* = 3 *Nrp1*^{fl/fl}; *Ly22*^{cre/+} sham; *n* = 5 *Nrp1*^{fl/fl}; *Ly22*^{cre/+} TAC. Data as mean ± SEM and analyzed by two-way ANOVA and Tukey post hoc. **p* < 0.05.

(F–H) Flow cytometry (F) and quantification of cardiac Ly6C^{lo}Timd4⁺Lyve-1⁺ RMs (G) and relative BrdU incorporation (H) in *Nrp1*^{fl/fl}; *Ly22*^{cre/+} and *Nrp1*^{fl/fl}; *Ly22*^{+/+} mice 4 days after TAC. *n* = 3 *Nrp1*^{fl/fl}; *Ly22*^{+/+} TAC; *n* = 4 *Nrp1*^{fl/fl}; *Ly22*^{cre/+} TAC. Data as mean ± SEM and analyzed by unpaired t test. **p* < 0.05, ***p* < 0.01.

(I and J) Serial LV echocardiography in basal condition and 1–2–4–8 weeks after TAC in *Nrp1*^{fl/fl}; *Ly22*^{cre/+} and *Nrp1*^{fl/fl}; *Ly22*^{+/+} mice. EF (I) and RWT (J) are shown. *n* = 6 *Nrp1*^{fl/fl}; *Ly22*^{+/+} TAC; *n* = 7 *Nrp1*^{fl/fl}; *Ly22*^{cre/+} TAC. Analysis was performed by two-way ANOVA and Sidak post hoc. ****p* < 0.001.

(K and L) Serial LV echocardiography in basal condition and 2–4 weeks after TAC in *Nrp1*^{fl/fl}; *Rosa26*^{LSL-RFP/+}; *Cx3cr1*^{Cre-ERT2/+} (RM^{RFP-ΔNrp1}) and *Rosa26*^{LSL-RFP/+}; *Cx3cr1*^{Cre-ERT2/+} (RM^{RFP}) mice. EF (K) and RWT (L) are shown. *n* = 6 RM^{RFP} TAC; *n* = 8 RM^{RFP-ΔNrp1} TAC. Data as mean ± SEM and analyzed by two-way ANOVA and Sidak post hoc. **p* < 0.05.

(M–N) Quantification of cardiac RFP⁺ RMs (Ly6C^{lo}Timd4⁺Lyve-1⁺) (M) and relative BrdU incorporation (N) in RM^{RFP-ΔNrp1} and RM^{RFP} mice 4 days after TAC. *n* = 3 RM^{RFP} TAC; *n* = 3 RM^{RFP-ΔNrp1} TAC. Data as mean ± SEM and analyzed by unpaired t test. ***p* < 0.01, ****p* < 0.001. Schematics were created with BioRender.com. See also Figure S7 and Table S6.



(legend on next page)

double-edged sword. In fact, while excessive fibrosis is harmful for the heart, its complete absence might be deleterious as well, making the LV unable to establish the adaptive response. In addition, fibrotic tissues in the heart differently impact cardiac function depending on the type and location of fibrosis itself.⁴⁰ Typically, systolic dysfunction is associated with replacement fibrosis, mainly occurring after myocardial infarction.⁴⁰ By contrast, interstitial and perivascular fibrosis perturb diastolic function by altering myocardial architecture with late effects on systolic function. However, while perivascular fibrosis causes microvascular dysfunction that worsens diastolic function,^{40,44} the interstitial fibrosis is associated with cardiomyocyte growth to help the myocardium to withstand stress.⁴⁰ Our data showed that all the collagen deposition induced by TAC appears as thick bands of interstitial fibrosis that are reduced in mice that do not have the spleen or the celiac ganglion innervation and is similar to what we previously observed in *Pgfr*^{-/-} mice.¹⁴ This observation pairs with the cardiac remodeling phenotype analyzed by echocardiography and shows an adaptive hypertrophic remodeling in TAC mice that is lost when the spleen or its innervation is removed. Further supporting a connection with the effect of neural-driven PIGF-NRP1 signaling in macrophages, the reduced fibrosis observed in splenectomized or denervated mice subjected to TAC was accompanied by loss of expansion in phagocytic and profibrotic CD206⁺ macrophages. Among the different subsets of macrophages that can contribute to cardiac fibrosis and, as a consequence, affect cardiac function,⁴⁵ a recent work demonstrated that CCR2⁺ monocyte-derived macrophages express interleukin (IL)-1 β to drive fibroblast activation and deleterious cardiac fibrosis in the human heart during HF.⁴⁶

While macrophages are highly specialized across different tissues and organs, it is possible to identify common patterns of markers that are suggestive of tissue-protective functions.⁴⁵ Recently, Takaoka and colleagues demonstrated that NRP1 is preferentially expressed in resident-like Lyve-1⁺ arterial macrophages that have atheroprotective functions, mediating the activation of biological pathways related to actin filament organization.⁴⁷ Collectively, these and our data support the hypothesis that NRP1⁺ RMs have an essential cardioprotective role.

Despite substantial improvement in hypertension treatment and control achieved in the past years, the prevalence of HTN-HD and its associated HF risk continues to rise.⁵ Hence, prevention of HF in patients with HTN-HD represents an unmet medical need, suggesting that diagnosis and treatment should not be limited to assessment of morphological and functional LV parameters and blood pressure control. Our results obtained in hypertensive subjects indicate that circulating amounts of PIGF, correlating with hypertension and cardiac hypertrophic remodeling, might be a potentially valuable biomarker of HTN-HD. In addition, we found that the expression of NRP1 in cardiac RMs is conserved in humans.

Together, data identify a multiorgan response to cardiac pressure overload established by the heart, central and peripheral nervous systems, and the spleen through the cardioprotective PIGF-NRP1 pathway.

Limitations of the study

Our study has shown that pressure overload sends a signal from the LV to the nervous system. Whether this signal is conveyed via neuropeptides or via direct afferent innervation remains to be determined. Additionally, our results identified an LV pressure overload-mediated release of PIGF in the spleen, depending on direct sympathetic innervation of the immune organ. However, further investigations are necessary to identify which are the splenic cells responding to the noradrenergic stimulation and producing PIGF. Cell-type-selective PIGF-deficient mice will be instrumental to address this unsolved issue. Finally, our results do not clarify the intracellular mechanisms activated by PIGF in cardiac NRP1⁺ RMs. While we cannot infer biological significance from the data available, we can hypothesize that the PIGF-NRP1 pathway influences mechanisms related to efferocytosis and the production of collagen and cardioprotective factors (like IGF-1), overall mediating adaptive cardiac growth during hypertension.

RESOURCE AVAILABILITY

Lead contact

Requests for further information and resources should be directed to and will be fulfilled by the lead contact, Daniela Carnevale (daniela.carnevale@uniroma1.it or daniela.carnevale@neuromed.it).

Figure 7. Neural-driven PIGF-NRP1 pathway promotes profibrotic RM expansion to support adaptive fibrosis and hypertrophic remodeling in overloaded LV

(A) Cardiac IGF-1 amounts in *Pgfr*^{-/-}, *Nrp1*^{fl/fl}, *Lyz2*^{cre/+} and WT mice 4 days after TAC and in WT sham mice. *n* = 8 sham; *n* = 11 WT TAC; *n* = 5 *Pgfr*^{-/-} TAC; *n* = 5 *Nrp1*^{fl/fl}, *Lyz2*^{cre/+} TAC. Data as mean \pm SEM and analyzed by one-way ANOVA and Tukey post hoc. **p* < 0.05, ***p* < 0.01.

(B–D) Flow cytometry (B) and quantification of CD206 expression in cardiac RMs (Ly6C^{hi}Timd4⁺ Lyve-1⁺) (C) and in Nrp1⁺ RMs (D) in *Pgfr*^{-/-}, *Nrp1*^{fl/fl}, *Lyz2*^{cre/+} and WT mice 4 days after TAC. *n* = 6 WT TAC; *n* = 3 *Pgfr*^{-/-} TAC; *n* = 3 *Nrp1*^{fl/fl}, *Lyz2*^{cre/+} TAC. Data as mean \pm SEM and analyzed by one-way ANOVA and Tukey post hoc. **p* < 0.05, ***p* < 0.01, ****p* < 0.001.

(E–G) Flow cytometry (E) and quantification of CD206 expression in cardiac RMs (F) and RM Nrp1⁺ (G) in mice subjected to TAC for 4 days and to splenectomy or CGX, and in control TAC mice. *n* = 5 TAC; *n* = 3 TAC –spleen; *n* = 3 TAC CGX. Data as mean \pm SEM and analyzed by one-way ANOVA and Tukey post hoc. **p* < 0.05.

(H and I) Fibrosis evaluation by picrosirius red analysis of heart sections from mice subjected to TAC or sham and to splenectomy (–spleen) or CGX, and relative control groups (Ctrl) (scale bar, 100 μ m). *n* = 4 sham ctrl; *n* = 4 sham –spleen; *n* = 4 sham CGX; *n* = 5 TAC ctrl; *n* = 4 TAC –spleen; *n* = 4 TAC CGX. Data as mean \pm SEM and analyzed by one-way ANOVA and Tukey post hoc. **p* < 0.05.

(J) Circulating amounts of PIGF in hypertensive patients (2–3rd tertiles) compared with normotensive patients (NT-1st). *n* = 15 NT-1st; *n* = 14 2–3rd. Data as mean \pm SEM and analyzed by Mann-Whitney test ***p* < 0.01.

(K) Pearson's correlation between CD68 and NRP1 in human myocardial tissues. **p* < 0.05.

(L and M) Immunofluorescence (L) and quantification (M) of NRP1 in cardiac CD68⁺CCR2⁺ RMs and in recruited CD68⁺CCR2⁺ macrophages in human cardiac biopsies from HF patients. Data as mean \pm SEM and analyzed by unpaired t test. ****p* < 0.001. Schematics were created with BioRender.com.

See also Table S7.

Materials availability

This study did not generate new unique reagents.

Data and code availability

This manuscript did not generate new code. All data and materials are available within the article, within the [supplemental information](#), or from the [lead contact](#) upon reasonable request.

ACKNOWLEDGMENTS

This work was funded by the ERA-CVD Consortium (NEMO-IMMUNEagainstHF) to D.C., S.E., T.P.M., and S.L.P. (German Ministry for Education and Research 01KL1901); Polish National Centre for Research and Development (ERA-CVD/NEMO/7/2019) to T.P.M.; the European Research Council (ERC-StG:759921-SymPATHY) to D.C.; the Italian Ministry of University (MUR) "PRIN2020-Competitive Research Projects of National Relevance" to D.C.; the Italian Ministry of Health (MoH) "Ricerca Corrente" to D.C. and G.L.; "Sapienza" Ateneo 2020_RG120172B9132731 to G.L.; and Biotechnology and Biological Sciences Research Council (BBSRC) grant (BB/Y005694/1) to G.D.

AUTHOR CONTRIBUTIONS

S.P. contributed to the experiments' design, data analysis and interpretation, and manuscript writing and performed and analyzed flow cytometry data. L.C. analyzed flow cytometry, electrophysiological recordings, echocardiographic data, and human databases; contributed to data analysis and interpretation; and performed statistical analysis. M.P. performed histological analysis and contributed to data analysis and interpretation and figure drafting. F.P. and V.F. performed surgeries, electrophysiological recordings, and echocardiographic analyses. A.M. generated and maintained transgenic colonies. S.F. performed histological and biochemical analyses. A.Z., J.P., R.C., and F.M. provided technical support. T.P.M., B.K., and T.J.G. performed analysis on human samples. S.N. and S.E. performed scRNA-seq analysis. G.D. performed FOS analysis and contributed to the design of viral tracing experiments. C.B. provided *Rosa26^{LSL-RFP/+};Cx3cr1^{Cre-ERT2/+}* mice. S.L.P. analyzed fibrosis. D.C. and G.L. conceived the study, obtained funding, supervised experiments, interpreted results, and wrote the manuscript. All authors reviewed and approved the manuscript.

DECLARATION OF INTERESTS

The authors declare no competing interests.

STAR★METHODS

Detailed methods are provided in the online version of this paper and include the following:

- [KEY RESOURCES TABLE](#)
- [METHODS DETAILS](#)
 - Animal studies
- [HUMAN STUDIES](#)
 - Ethics committee
 - Gene expression measurements in cardiac biopsies
 - Statistical analysis
 - Immunofluorescence analyses of cardiac biopsies
 - Quantification of circulating amount of PIGF

SUPPLEMENTAL INFORMATION

Supplemental information can be found online at <https://doi.org/10.1016/j.immuni.2025.02.013>.

Received: October 24, 2024

Revised: February 6, 2025

Accepted: February 10, 2025

Published: February 28, 2025

REFERENCES

1. Coffman, T.M. (2011). Under pressure: the search for the essential mechanisms of hypertension. *Nat. Med.* 17, 1402–1409. <https://doi.org/10.1038/nm.2541>.
2. Whelton, P.K., Carey, R.M., Aronow, W.S., Casey, D.E., Jr., Collins, K.J., Dennison Himmelfarb, C., DePalma, S.M., Gidding, S., Jamerson, K.A., Jones, D.W., et al. (2018). 2017 ACC/AHA/AAPA/ABC/ACPM/AGS/APhA/ASH/ASPC/NMA/PCNA guideline for the prevention, detection, evaluation, and management of high blood pressure in adults: executive summary: A report of the American College of Cardiology/American Heart Association Task Force on Clinical Practice guidelines. *Hypertension* 71, 1269–1324. <https://doi.org/10.1161/HYP.000000000000066>.
3. Padwal, R.S., Bienek, A., McAlister, F.A., and Campbell, N.R.C.; Outcomes Research Task Force; Canadian Hypertension Education Program (2016). Epidemiology of hypertension in Canada: an update. *Can. J. Cardiol.* 32, 687–694. <https://doi.org/10.1016/j.cjca.2015.07.734>.
4. Lozano, R., Naghavi, M., Foreman, K., Lim, S., Shibuya, K., Aboyans, V., Abraham, J., Adair, T., Aggarwal, R., Ahn, S.Y., et al. (2012). Global and regional mortality from 235 causes of death for 20 age groups in 1990 and 2010: a systematic analysis for the Global Burden of Disease Study 2010. *Lancet* 380, 2095–2128. [https://doi.org/10.1016/S0140-6736\(12\)61728-0](https://doi.org/10.1016/S0140-6736(12)61728-0).
5. Díez, J., and Butler, J. (2023). Growing heart failure Burden of hypertensive heart disease: A call to action. *Hypertension* 80, 13–21. <https://doi.org/10.1161/HYPERTENSIONAHA.122.19373>.
6. Ezekowitz, J.A., O'Meara, E., McDonald, M.A., Abrams, H., Chan, M., Ducharme, A., Giannetti, N., Grzeslo, A., Hamilton, P.G., Heckman, G.A., et al. (2017). 2017 comprehensive update of the Canadian Cardiovascular Society guidelines for the management of heart failure. *Can. J. Cardiol.* 33, 1342–1433. <https://doi.org/10.1016/j.cjca.2017.08.022>.
7. Claeys, M.J., Mullens, W., Vandekerckhove, Y., Duytschaever, M., De Maeyer, C., and Pasquet, A. (2017). Summary of 2016 ESC guidelines on heart failure, atrial fibrillation, dyslipidaemia and cardiovascular prevention. *Acta Cardiol.* 72, 610–615. <https://doi.org/10.1080/00015385.2017.1319681>.
8. Messerli, F.H., Rimoldi, S.F., and Bangalore, S. (2017). The transition from hypertension to heart failure: contemporary update. *JACC Heart Fail.* 5, 543–551. <https://doi.org/10.1016/j.jchf.2017.04.012>.
9. Carnevale, D., and Lembo, G. (2021). Neuroimmune interactions in cardiovascular diseases. *Cardiovasc. Res.* 117, 402–410. <https://doi.org/10.1093/cvr/cvaa151>.
10. Adamo, L., Rocha-Resende, C., Prabhu, S.D., and Mann, D.L. (2020). Reappraising the role of inflammation in heart failure. *Nat. Rev. Cardiol.* 17, 269–285. <https://doi.org/10.1038/s41569-019-0315-x>.
11. Hartupee, J., and Mann, D.L. (2017). Neurohormonal activation in heart failure with reduced ejection fraction. *Nat. Rev. Cardiol.* 14, 30–38. <https://doi.org/10.1038/nrcardio.2016.163>.
12. Malpas, S.C. (2010). Sympathetic nervous system overactivity and its role in the development of cardiovascular disease. *Physiol. Rev.* 90, 513–557. <https://doi.org/10.1152/physrev.00007.2009>.
13. Rockman, H.A., Wachhorst, S.P., Mao, L., and Ross, J., Jr. (1994). ANG II receptor blockade prevents ventricular hypertrophy and ANF gene expression with pressure overload in mice. *Am. J. Physiol.* 266, H2468–H2475. <https://doi.org/10.1152/ajpheart.1994.266.6.H2468>.
14. Carnevale, D., Cifelli, G., Mascio, G., Madonna, M., Sbroglio, M., Perrino, C., Persico, M.G., Frati, G., and Lembo, G. (2011). Placental growth factor regulates cardiac inflammation through the tissue inhibitor of metalloproteinases-3/tumor necrosis factor- α -converting enzyme axis: crucial role for adaptive cardiac remodeling during cardiac pressure overload. *Circulation* 124, 1337–1350. <https://doi.org/10.1161/CIRCULATIONAHA.111.050500>.
15. Rockman, H.A., Ross, R.S., Harris, A.N., Knowlton, K.U., Steinhilber, M.E., Field, L.J., Ross, J., Jr., and Chien, K.R. (1991). Segregation of atrial-specific and inducible expression of an atrial natriuretic factor

- transgene in an in vivo murine model of cardiac hypertrophy. *Proc. Natl. Acad. Sci. USA* 88, 8277–8281. <https://doi.org/10.1073/pnas.88.18.8277>.
16. Dick, S.A., Macklin, J.A., Nejat, S., Momen, A., Clemente-Casares, X., Althagafi, M.G., Chen, J., Kantores, C., Hosseinzadeh, S., Aronoff, L., et al. (2019). Self-renewing resident cardiac macrophages limit adverse remodeling following myocardial infarction. *Nat. Immunol.* 20, 29–39. <https://doi.org/10.1038/s41590-018-0272-2>.
17. Epelman, S., Lavine, K.J., Beaudin, A.E., Sojka, D.K., Carrero, J.A., Calderon, B., Brija, T., Gautier, E.L., Ivanov, S., Satpathy, A.T., et al. (2014). Embryonic and adult-derived resident cardiac macrophages are maintained through distinct mechanisms at steady state and during inflammation. *Immunity* 40, 91–104. <https://doi.org/10.1016/j.immuni.2013.11.019>.
18. Wong, N.R., Mohan, J., Kopecky, B.J., Guo, S., Du, L., Leid, J., Feng, G., Lokshina, I., Dmytrenko, O., Luehmann, H., et al. (2021). Resident cardiac macrophages mediate adaptive myocardial remodeling. *Immunity* 54, 2072–2088.e7. <https://doi.org/10.1016/j.immuni.2021.07.003>.
19. Revelo, X.S., Parthiban, P., Chen, C., Barrow, F., Fredrickson, G., Wang, H., Yücel, D., Herman, A., and van Berlo, J.H. (2021). Cardiac resident macrophages prevent fibrosis and stimulate angiogenesis. *Circ. Res.* 129, 1086–1101. <https://doi.org/10.1161/CIRCRESAHA.121.319737>.
20. Patel, B., Bansal, S.S., Ismail, M.A., Hamid, T., Rokosh, G., Mack, M., and Prabhu, S.D. (2018). CCR2(+) monocyte-derived infiltrating macrophages are required for adverse cardiac remodeling during pressure overload. *JACC Basic Transl. Sci.* 3, 230–244. <https://doi.org/10.1016/j.jacbts.2017.12.006>.
21. Carnevale, D. (2022). Neuroimmune axis of cardiovascular control: mechanisms and therapeutic implications. *Nat. Rev. Cardiol.* 19, 379–394. <https://doi.org/10.1038/s41569-022-00678-w>.
22. Swirski, F.K., and Nahrendorf, M. (2018). Cardioimmunology: the immune system in cardiac homeostasis and disease. *Nat. Rev. Immunol.* 18, 733–744. <https://doi.org/10.1038/s41577-018-0065-8>.
23. Heusch, G., and Kleinbongard, P. (2025). The spleen in ischaemic heart disease. *Nat. Rev. Cardiol.* <https://doi.org/10.1038/s41569-024-01114-x>.
24. Carnevale, D., Pallante, F., Fardella, V., Fardella, S., Iacobucci, R., Federici, M., Cifelli, G., De Lucia, M., and Lembo, G. (2014). The angiogenic factor PIGF mediates a neuroimmune interaction in the spleen to allow the onset of hypertension. *Immunity* 41, 737–752. <https://doi.org/10.1016/j.immuni.2014.11.002>.
25. Carnevale, L., Pallante, F., Perrotta, M., Iodice, D., Perrotta, S., Fardella, S., Mastroiacovo, F., Carnevale, D., and Lembo, G. (2020). Celiac vagus nerve stimulation recapitulates angiotensin II-induced splenic noradrenergic activation, driving egress of CD8 effector cells. *Cell Rep.* 33, 108494. <https://doi.org/10.1016/j.celrep.2020.108494>.
26. Nickel, A.G., von Hardenberg, A., Hohl, M., Löffler, J.R., Kohlhaas, M., Becker, J., Reil, J.C., Kazakov, A., Bonnekoh, J., Stadelmaier, M., et al. (2015). Reversal of mitochondrial transhydrogenase causes oxidative stress in heart failure. *Cell Metab.* 22, 472–484. <https://doi.org/10.1016/j.cmet.2015.07.008>.
27. Zaman, R., Hamidzadeh, H., Kantores, C., Wong, A., Dick, S.A., Wang, Y., Momen, A., Aronoff, L., Lin, J., Razani, B., et al. (2021). Selective loss of resident macrophage-derived insulin-like growth factor-1 abolishes adaptive cardiac growth to stress. *Immunity* 54, 2057–2071.e6. <https://doi.org/10.1016/j.immuni.2021.07.006>.
28. Fujiu, K., Shibata, M., Nakayama, Y., Ogata, F., Matsumoto, S., Noshita, K., Iwami, S., Nakae, S., Komuro, I., Nagai, R., et al. (2017). A heart-brain-kidney network controls adaptation to cardiac stress through tissue macrophage activation. *Nat. Med.* 23, 611–622. <https://doi.org/10.1038/nm.4326>.
29. Koren, T., Yifa, R., Amer, M., Krot, M., Boshnak, N., Ben-Shaanan, T.L., Azulay-Debby, H., Zalayat, I., Avishai, E., Hajjo, H., et al. (2021). Insular cortex neurons encode and retrieve specific immune responses. *Cell* 184, 6211. <https://doi.org/10.1016/j.cell.2021.11.021>.
30. Chavan, S.S., Pavlov, V.A., and Tracey, K.J. (2017). Mechanisms and therapeutic relevance of neuro-immune communication. *Immunity* 46, 927–942. <https://doi.org/10.1016/j.immuni.2017.06.008>.
31. Prescott, S.L., and Liberles, S.D. (2022). Internal senses of the vagus nerve. *Neuron* 110, 579–599. <https://doi.org/10.1016/j.neuron.2021.12.020>.
32. Carnevale, D., Perrotta, M., Pallante, F., Fardella, V., Iacobucci, R., Fardella, S., Carnevale, L., Carnevale, R., De Lucia, M., Cifelli, G., et al. (2016). A cholinergic-sympathetic pathway primes immunity in hypertension and mediates brain-to-spleen communication. *Nat. Commun.* 7, 13035. <https://doi.org/10.1038/ncomms13035>.
33. Perrotta, M., Lori, A., Carnevale, L., Fardella, S., Cifelli, G., Iacobucci, R., Mastroiacovo, F., Iodice, D., Pallante, F., Storto, M., et al. (2018). Deoxycorticosterone acetate-salt hypertension activates placental growth factor in the spleen to couple sympathetic drive and immune system activation. *Cardiovasc. Res.* 114, 456–467. <https://doi.org/10.1093/cvr/cvy001>.
34. Kressel, A.M., Tsaava, T., Levine, Y.A., Chang, E.H., Addorisio, M.E., Chang, Q., Burbach, B.J., Carnevale, D., Lembo, G., Zador, A.M., et al. (2020). Identification of a brainstem locus that inhibits tumor necrosis factor. *Proc. Natl. Acad. Sci. USA* 117, 29803–29810. <https://doi.org/10.1073/pnas.2008213117>.
35. Ziegler, K.A., Ahles, A., Wille, T., Kerler, J., Ramanujam, D., and Engelhardt, S. (2018). Local sympathetic denervation attenuates myocardial inflammation and improves cardiac function after myocardial infarction in mice. *Cardiovasc. Res.* 114, 291–299. <https://doi.org/10.1093/cvr/cvx227>.
36. Hilgendorf, I., Gerhardt, L.M.S., Tan, T.C., Winter, C., Holderried, T.A.W., Chousterman, B.G., Iwamoto, Y., Liao, R., Zirk, A., Scherer-Crosbie, M., et al. (2014). Ly-6C^{high} monocytes depend on Nr4a1 to balance both inflammatory and reparative phases in the infarcted myocardium. *Circ. Res.* 114, 1611–1622. <https://doi.org/10.1161/CIRCRESAHA.114.303204>.
37. Snuderl, M., Batista, A., Kirkpatrick, N.D., Ruiz de Almodovar, C., Riedemann, L., Walsh, E.C., Anolik, R., Huang, Y., Martin, J.D., Kamoun, W., et al. (2013). Targeting placental growth factor/neuropilin 1 pathway inhibits growth and spread of medulloblastoma. *Cell* 152, 1065–1076. <https://doi.org/10.1016/j.cell.2013.01.036>.
38. Prud'homme, G.J., and Glinka, Y. (2012). Neuropilins are multifunctional coreceptors involved in tumor initiation, growth, metastasis and immunity. *Oncotarget* 3, 921–939. <https://doi.org/10.18632/oncotarget.626>.
39. Dick, S.A., Wong, A., Hamidzadeh, H., Nejat, S., Nechanitzky, R., Vohra, S., Mueller, B., Zaman, R., Kantores, C., Aronoff, L., et al. (2022). Three tissue resident macrophage subsets coexist across organs with conserved origins and life cycles. *Sci. Immunol.* 7, eabf7777. <https://doi.org/10.1126/sciimmunol.abf7777>.
40. Frangogiannis, N.G. (2021). Cardiac fibrosis. *Cardiovasc. Res.* 117, 1450–1488. <https://doi.org/10.1093/cvr/cvaa324>.
41. Mohanta, S.K., Peng, L., Li, Y., Lu, S., Sun, T., Carnevale, L., Perrotta, M., Ma, Z., Förster, B., Stanic, K., et al. (2022). Neuroimmune cardiovascular interfaces control atherosclerosis. *Nature* 605, 152–159. <https://doi.org/10.1038/s41586-022-04673-6>.
42. Wagner, J.U.G., Tombor, L.S., Malacarne, P.F., Kettenhausen, L.M., Panthel, J., Kujundzic, H., Manickam, N., Schmitz, K., Cipca, M., Stolz, K.A., et al. (2023). Aging impairs the neurovascular interface in the heart. *Science* 381, 897–906. <https://doi.org/10.1126/science.ade4961>.
43. Ziegler, K.A., Ahles, A., Dueck, A., Esfandiyari, D., Pichler, P., Weber, K., Kotschi, S., Bartelt, A., Sinicina, I., Graw, M., et al. (2023). Immune-mediated denervation of the pineal gland underlies sleep disturbance in cardiac disease. *Science* 381, 285–290. <https://doi.org/10.1126/science.abn6366>.
44. Dai, Z., Aoki, T., Fukumoto, Y., and Shimokawa, H. (2012). Coronary perivascular fibrosis is associated with impairment of coronary blood flow in patients with non-ischemic heart failure. *J. Cardiol.* 60, 416–421. <https://doi.org/10.1016/j.jicc.2012.06.009>.
45. Yang, S., Penna, V., and Lavine, K.J. (2025). Functional diversity of cardiac macrophages in health and disease. *Nat. Rev. Cardiol.* <https://doi.org/10.1038/s41569-024-01109-8>.

46. Amrute, J.M., Luo, X., Penna, V., Yang, S., Yamawaki, T., Hayat, S., Bredemeyer, A., Jung, I.H., Kadyrov, F.F., Heo, G.S., et al. (2024). Targeting immune-fibroblast cell communication in heart failure. *Nature* 635, 423–433. <https://doi.org/10.1038/s41586-024-08008-5>.
47. Takaoka, M., Zhao, X., Lim, H.Y., Magnussen, C.G., Ang, O., Suffee, N., Schrank, P.R., Ong, W.S., Tsiantoulas, D., Sommer, F., et al. (2024). Early intermittent hyperlipidaemia alters tissue macrophages to fuel atherosclerosis. *Nature* 634, 457–465. <https://doi.org/10.1038/s41586-024-07993-x>.
48. Gigante, B., Morlino, G., Gentile, M.T., Persico, M.G., and De Falco, S. (2006). Plgf^{-/-}eNos^{-/-} mice show defective angiogenesis associated with increased oxidative stress in response to tissue ischemia. *FASEB J.* 20, 970–972. <https://doi.org/10.1096/fj.05-4481fje>.
49. McKendrick, J.G., Jones, G.R., Elder, S.S., Watson, E., T'Jonck, W., Mercer, E., Magalhaes, M.S., Rocchi, C., Hegarty, L.M., Johnson, A.L., et al. (2023). CSF1R-dependent macrophages in the salivary gland are essential for epithelial regeneration after radiation-induced injury. *Sci. Immunol.* 8, eadd4374. <https://doi.org/10.1126/sciimmunol.eadd4374>.
50. Stuart, T., Butler, A., Hoffman, P., Hafemeister, C., Papalexi, E., Mauck, W.M., 3rd, Hao, Y., Stoeckius, M., Smibert, P., and Satija, R. (2019). Comprehensive integration of single-cell data. *Cell* 177, 1888–1902.e21. <https://doi.org/10.1016/j.cell.2019.05.031>.
51. Stuart, T., and Satija, R. (2019). Integrative single-cell analysis. *Nat. Rev. Genet.* 20, 257–272. <https://doi.org/10.1038/s41576-019-0093-7>.
52. Fliegner, D., Schubert, C., Penkalla, A., Witt, H., Kararigas, G., Dworatzek, E., Staub, E., Martus, P., Ruiz Noppinger, P., Kintscher, U., et al. (2010). Female sex and estrogen receptor-beta attenuate cardiac remodeling and apoptosis in pressure overload. *Am. J. Physiol. Regul. Integr. Comp. Physiol.* 298, R1597–R1606. <https://doi.org/10.1152/ajpregu.00825.2009>.
53. Lee, S.L., Wesselschmidt, R.L., Linette, G.P., Kanagawa, O., Russell, J.H., and Milbrandt, J. (1995). Unimpaired thymic and peripheral T cell death in mice lacking the nuclear receptor NGFI-B (Nur77). *Science* 269, 532–535. <https://doi.org/10.1126/science.7624775>.
54. Boring, L., Gosling, J., Chensue, S.W., Kunkel, S.L., Farese, R.V., Jr., Broxmeyer, H.E., and Charo, I.F. (1997). Impaired monocyte migration and reduced type 1 (Th1) cytokine responses in C-C chemokine receptor 2 knockout mice. *J. Clin. Invest.* 100, 2552–2561. <https://doi.org/10.1172/JCI119798>.
55. Jung, S., Aliberti, J., Graemmel, P., Sunshine, M.J., Kreutzberg, G.W., Sher, A., and Littman, D.R. (2000). Analysis of fractalkine receptor CX(3)CR1 function by targeted deletion and green fluorescent protein reporter gene insertion. *Mol. Cell. Biol.* 20, 4106–4114. <https://doi.org/10.1128/MCB.20.11.4106-4114.2000>.
56. Gu, C., Rodriguez, E.R., Reimert, D.V., Shu, T., Fritzsche, B., Richards, L.J., Kolodkin, A.L., and Ginty, D.D. (2003). Neuropilin-1 conveys semaphorin and VEGF signaling during neural and cardiovascular development. *Dev. Cell* 5, 45–57. [https://doi.org/10.1016/s1534-5807\(03\)00169-2](https://doi.org/10.1016/s1534-5807(03)00169-2).
57. Clausen, B.E., Burkhardt, C., Reith, W., Renkawitz, R., and Förster, I. (1999). Conditional gene targeting in macrophages and granulocytes using LysMcre mice. *Transgen. Res.* 8, 265–277. <https://doi.org/10.1023/a:1008942828960>.
58. Brancaccio, M., Fratta, L., Notte, A., Hirsch, E., Poulet, R., Guazzone, S., De Acetis, M., Vecchione, C., Marino, G., Altruda, F., et al. (2003). Melusin, a muscle-specific integrin beta1-interacting protein, is required to prevent cardiac failure in response to chronic pressure overload. *Nat. Med.* 9, 68–75. <https://doi.org/10.1038/nm805>.
59. Patrucco, E., Notte, A., Barberis, L., Selvetella, G., Maffei, A., Brancaccio, M., Marengo, S., Russo, G., Azzolino, O., Rybalkin, S.D., et al. (2004). PI3Kgamma modulates the cardiac response to chronic pressure overload by distinct kinase-dependent and -independent effects. *Cell* 118, 375–387. <https://doi.org/10.1016/j.cell.2004.07.017>.
60. Carnevale, D., Mascio, G., D'Andrea, I., Fardella, V., Bell, R.D., Branchi, I., Pallante, F., Zlokovic, B., Yan, S.S., and Lembo, G. (2012). Hypertension induces brain beta-amyloid accumulation, cognitive impairment, and memory deterioration through activation of receptor for advanced glycation end products in brain vasculature. *Hypertension* 60, 188–197. <https://doi.org/10.1161/HYPERTENSIONAHA.112.195511>.
61. D'Andrea, I., Fardella, V., Fardella, S., Pallante, F., Ghigo, A., Iacobucci, R., Maffei, A., Hirsch, E., Lembo, G., and Carnevale, D. (2015). Lack of kinase-independent activity of PI3Kgamma in locus coeruleus induces ADHD symptoms through increased CREB signaling. *EMBO Mol. Med.* 7, 904–917. <https://doi.org/10.15252/emmm.201404697>.
62. Carnevale, L., D'Angelosante, V., Landolfi, A., Grillea, G., Selvetella, G., Storto, M., Lembo, G., and Carnevale, D. (2018). Brain MRI fiber-tracking reveals white matter alterations in hypertensive patients without damage at conventional neuroimaging. *Cardiovasc. Res.* 114, 1536–1546. <https://doi.org/10.1093/cvr/cvy104>.
63. Carnevale, L., Maffei, A., Landolfi, A., Grillea, G., Carnevale, D., and Lembo, G. (2020). Brain functional magnetic resonance imaging highlights altered connections and functional networks in patients with hypertension. *Hypertension* 76, 1480–1490. <https://doi.org/10.1161/HYPERTENSIONAHA.120.15296>.

STAR★METHODS

KEY RESOURCES TABLE

REAGENT or RESOURCE	SOURCE	IDENTIFIER
Antibodies		
Purified Rat Anti-Mouse CD16/CD32 (Mouse BD Fc Block) (clone 2.4G2)	BD Pharmigen	Cat# 553142; RRID: AB_394657
Monoclonal anti-mouse CD45 - BUV395 conjugated (clone 30-F11)	BD Horizon	Cat# 564279; RRID: AB_2651134
Monoclonal anti-mouse CD45 - APC-Cy7 conjugated (clone 30-F11)	BD Pharmigen	Cat# 557659; RRID: AB_396774
Monoclonal anti-mouse CD11b - BUV737 conjugated (clone M1/70)	BD Horizon	Cat# 612800; RRID: AB_2870127
Monoclonal anti-mouse CD11b - PE conjugated (clone M1/70)	BD Pharmigen	Cat# 553311; RRID: AB_396680
Monoclonal anti-mouse Timd4 - BV711 conjugated (clone RMT4-54)	BD OptiBuild	Cat# 745509; RRID: AB_2743044
Monoclonal anti-mouse Ly6G - BV510 conjugated (clone 1A8)	BD OptiBuild	Cat# 740157; RRID: AB_2739910
Monoclonal anti-mouse Bromodeoxyuridine (BrdU) PerCP-Cy5.5 - conjugated (clone 3D4)	BD Pharmigen	Cat# 560809; RRID: AB_2033929
True-Stain Monocyte Blocker monocyte blocker	BioLegend	Cat# 426103
Monoclonal anti-mouse CD64 - BV605 conjugated (clone X54-5/7.1)	BioLegend	Cat# 139323; RRID: AB_2629778
Monoclonal anti-mouse Ly6C - BV421 conjugated (clone HK1.4)	BioLegend	Cat# 128032; RRID: AB_2562178
Monoclonal anti-mouse Ly6C - FITC conjugated (clone HK1.4)	BioLegend	Cat# 128006; RRID: AB_1186135
Monoclonal anti-mouse CD206 - PE-Dazzle594 conjugated (clone C068C2)	BioLegend	Cat# 141732; RRID: AB_2565931
Monoclonal anti-mouse Lyve1 - eFluor-450 conjugated (clone ALY7)	eBioscience	Cat# 48-0443-82; RRID: AB_2784723
Polyclonal anti-mouse/rat Neuropilin-1 - PE conjugated	R&D Systems	Cat# FAB566P; RRID: AB_10890913
Polyclonal anti-mouse/rat Neuropilin-1 - APC conjugated	R&D Systems	Cat# FAB566A; RRID: AB_2267476
Rabbit anti-mouse PIGF	Abcam	Cat# ab9542; RRID: AB_307330
Rabbit anti-mouse c-FOS	Abcam	Cat# ab190289; RRID: AB_2737414
Rabbit anti-beta III Tubulin - Neuronal marker	Abcam	Cat# ab18207; RRID: AB_444319
Alexa Fluor 594 Donkey Anti-Rabbit IgG (H+L)	Abcam	Cat# ab150076; RRID: AB_2782993
Rabbit anti-CCR2	Abcam	Cat# ab32144; RRID: AB_1603737
Rat anti-mouse ERT-R7	Acris	Cat# BM4018; RRID: AB_981318
Rat anti-mouse CD169	Biorad	Cat# MCA884; RRID: AB_322416
Mouse anti-human CD68	Biorad	Cat# MCA5709; RRID: AB_11152768
Sheep anti-mouse Tyrosine Hydroxylase (TH)	Millipore	Cat# AB1542; RRID: AB_90755
Rabbit anti-mouse Tyrosine Hydroxylase (TH)	Millipore	Cat# AB152; RRID: AB_390204
Mouse anti-human Neuropilin-1	Santa Cruz	Cat# sc-5307; RRID: AB_2282634
Isolectin GS-IB4 - Alexa Fluor 488 conjugate	Invitrogen	Cat# I21411; RRID: AB_2314662
Streptavidin - Alexa Fluor 488 conjugate	Invitrogen	Cat# S32354; RRID: AB_2315383
Horse Anti-Rabbit IgG (H+L) - Biotinylated	Vector Laboratories	Cat# BA-1100; RRID: AB_2336201
Alexa Fluor 488 Donkey Anti-Rat IgG (H+L)	Jackson ImmunoResearch	Cat# 712-545-153; RRID: AB_2340684
Alexa Fluor 488 Donkey Anti-Rabbit IgG (H+L)	Jackson ImmunoResearch	Cat# 711-545-152; RRID: AB_2313584
Cy3 Donkey Anti-Sheep IgG (H+L)	Jackson ImmunoResearch	Cat# 713-165-003; RRID: AB_2340727
Cy3 Donkey Anti-Rat IgG (H+L)	Jackson ImmunoResearch	Cat# 712-165-153; RRID: AB_2340667
Cy3 Donkey Anti-Rabbit IgG (H+L)	Jackson ImmunoResearch	Cat# 711-165-152; RRID: AB_2307443
F(ab') ₂ fragment Goat anti-Mouse IgG (H+L)	Jackson ImmunoResearch	Cat# 115-007-003; RRID: AB_2338476
Alexa Fluor 647 Donkey Anti-Goat IgG (H+L)	Jackson ImmunoResearch	Cat# 705-605-147; RRID: AB_2340437
Alexa Fluor 488 Donkey Anti-Mouse IgG (H+L)	Jackson ImmunoResearch	Cat# 715-545-150; RRID: AB_2340846
Chemicals, peptides, and recombinant proteins		
Collagenase from Clostridium histolyticum, Type I	Sigma-Aldrich	Cat# C0130
Hyaluronidase from bovine, Type I-S	Sigma-Aldrich	Cat# H3506
DNase I from bovine pancreas	Sigma-Aldrich	Cat# D5025

(Continued on next page)

Continued

REAGENT or RESOURCE	SOURCE	IDENTIFIER
DNase I from bovine pancreas	Sigma-Aldrich	Cat# D4513
Direct Red 80 - Dye content 25%	Sigma-Aldrich	Cat# 365548
Bovine Serum Albumin (BSA)	Sigma-Aldrich	Cat# A3059
Sodium azide	Sigma-Aldrich	Cat# 71289
Ethylenediaminetetraacetic acid disodium salt dihydrate (EDTA)	Sigma-Aldrich	Cat# E5134
Quick-hardening mounting medium (Eukitt)	Sigma-Aldrich	Cat# 03989
Polyvinyl alcohol mounting medium with DABCO, antifading	Sigma-Aldrich	Cat# 10981
Donkey serum	Sigma-Aldrich	Cat# D9663-10ML
Bromodeoxyuridine (BrdU)	BD Bioscience	Cat# 550891
Recombinant Mouse PlGF-2 Protein	R&D Systems	Cat# 465-PL-050
O.C.T. compound	Bio-Optica	Cat# 05-9801
4',6-Diamidino-2-Phenylindole (DAPI) solution	Invitrogen	Cat# 62248
Dulbecco's Modified Eagle Medium (DMEM)	Gibco	Cat# 21969-035
Hank's Balanced Salt Solution HBSS	Gibco	Cat# 24020-091
Heat inactivated Fetal Bovine Serum (FBS)	Gibco	Cat# 10082-147
Critical commercial assays		
Mouse PlGF-2 Quantikine ELISA Kit	R&D Systems	Cat# MP200
Mouse/Rat IGF-1 Quantikine ELISA kit	R&D Systems	Cat# MG100
Human PlGF ELISA Kit	Abcam	Cat# ab100629
TaqMan Gene Expression Assays for Neuropilin-1	Thermo Fisher Scientific	Assay ID# Hs00826128_m1
TaqMan Gene Expression Assays for CD68	Thermo Fisher Scientific	Assay ID# Hs02836816_g1
Experimental models: Organisms/strains		
Mouse: C57Bl/6J	The Jackson Laboratory	Cat# 000664; RRID:IMSR_JAX:000664
Mouse: <i>Pgfr</i> ^{-/-}	Gigante et al. ⁴⁸ ; Carnevale et al. ¹⁴ ; Carnevale et al. ²⁴ ; Perrotta et al. ³³	N/A
Mouse: <i>Nr4a1</i> ^{tm1Jm1/J}	The Jackson Laboratory	Cat# 006187; RRID:IMSR_JAX:006187
Mouse: <i>Ccr2</i> ^{tm1Ifc/J}	The Jackson Laboratory	Cat# 004999; RRID:IMSR_JAX:004999
Mouse: <i>Cx3cr1</i> ^{tm1Litt/J}	The Jackson Laboratory	Cat# 005582; RRID:IMSR_JAX:005582
Mouse: <i>Nrp1</i> ^{tm2Ddg/J} , <i>Nrp1</i> ^{fl/fl}	The Jackson Laboratory	Cat# 005247; RRID:IMSR_JAX:005247
Mouse: <i>Lyz2</i> ^{tm1(Cre)Ifc/J}	The Jackson Laboratory	Cat# 004781; RRID:IMSR_JAX:004781
Mouse: <i>Rosa26</i> ^{LSL-RFP/+} ; <i>Cx3cr1</i> ^{Cre-ERT2/+}	McKendrick et al. ⁴⁹	N/A
Software and algorithms		
BD FACSDiva Software v8.0.1.1	BD Bioscience	https://www.bdbiosciences.com/
SpectroFlo Software v3.3.0	Cytek	https://cytekbio.com/pages/spectro-flo
FlowJo Software v10.8.1	FlowJo, LLC	https://www.flowjo.com/
Vevo Lab Visualsonics	Visualsonics	https://www.visualsonics.com/
Lab Chart 7 (Spike Analysis Module)	ADInstruments	https://www.adinstruments.com/products/spike-histogram
MATLAB	MathWorks	https://it.mathworks.com/?s_tid=gn_logo
GraphPad Prism v7.00	GraphPad	https://www.graphpad.com/
GraphPad Prism v9.1.0	GraphPad	https://www.graphpad.com/
Seurat v3.1	Stuart et al. ⁵⁰ ; Stuart and Satija ⁵¹	https://github.com/satijalab/seurat
SPSS Statistics v23.0	IBM	https://www.ibm.com/support/pages/downloading-ibm-spss-statistics-23
SPSS Statistics v28.0.1.0	IBM	https://www.ibm.com/support/pages/downloading-ibm-spss-statistics-28010

(Continued on next page)

Continued

REAGENT or RESOURCE	SOURCE	IDENTIFIER
Other		
Fixation/Permeabilization Solution Kit (Cytofix/Cytoperm)	BD Cytofix/Cytoperm Plus	Cat# 555028
BD Lysing buffer	BD PharmLyse	Cat# 555899
Brilliant Stain Buffer	BD Horizon	Cat# 566349
Anti-Rat and Anti-Hamster Ig κ /Negative Control Compensation Particles Set	BD CompBeads	Cat# 552845
Anti-Mouse Ig, κ /Negative Control Compensation Particles Set	BD CompBeads	Cat# 552843
Direct-zol RNA Miniprep kit	Zymo Research	Cat# R2052
High-Capacity cDNA Reverse Transcription Kit	Applied Biosystems, USA	Cat# 4368814

METHODS DETAILS

Animal studies

Mice

All animal handling and experimental procedures were performed according to the European Community guidelines (EC Council Directive 2010/63) and the Italian legislation on animal experimentation (Decreto Legislativo D.Lgs 26/2014) and approved by our Institutional Ethic Committee and by the Italian Ministry of Health, Section for veterinary ethics and animal care/use. All efforts were made to minimize suffering, and the principles of Replacement, Reduction and Refinement (i.e., the “three Rs”) were applied to all experiments. Mice on a C57BL/6J background, aged 8–12 weeks, were used. Housing conditions were as follows: room temperature of 22 °C \pm 2 °C; 55% \pm 10% humidity; a 12 h light/dark cycle (light time, 6 am – 6 pm); sawdust as bedding; pellet food and tap water *ad libitum*. Since it has been demonstrated that male and female mice differently respond to cardiac pressure overload, only male mice were used in all the experiments in order to reduce the animal required to obtain homogeneous groups.⁵²

Mouse strains used included: C57BL/6J mice (The Jackson Laboratory stock number 000664), PlGF deficient (*Pgf*^{−/−}) mice with a homozygous deletion of the gene encoding for Placental Growth Factor^{14,24,33,48}; NR4a1 deficient (*Nr4a1*^{−/−}) mice with a homozygous deletion of the orphan nuclear hormone receptor – nuclear receptor subfamily 4 group a member 1 (*Nr4a1*^{tm1Jmi/J}, The Jackson Laboratory stock number 006187)⁵³; *Ccr2* deficient (*Ccr2*^{−/−}) mice with a homozygous deletion of the receptor of Monocyte Chemoattractant Protein (MCP)-1 (*Ccr2*^{tm1ffo/J}, The Jackson Laboratory stock number 004999)⁵⁴; *Cx3cr1* deficient (*Cx3cr1*^{−/−}) mice lacking the CX(3)-C motif chemokine receptor 1, the high-affinity functional chemokine receptor for fractalkine (CX3CL1) (*Cx3cr1*^{tm1Litt/J}, The Jackson Laboratory stock number 005582)⁵⁵; *Nrp1*^{fl/fl}; *Lyz2-cre* mice, a conditional transgenic mouse model with a selective deletion of *Nrp1* in myeloid lineage obtained by crossing mouse with *Nrp1* gene flanked by LoxP sequences (*Nrp1*^{tm2Ddg/J}, *Nrp1*^{fl/fl}, The Jackson Laboratory stock number 005247)⁵⁶ with mouse with a cre recombinase under the lysozyme M (*Lyz2*) promoter (*Lyz2*^{tm1(cre)lfo/J}, *Lyz2-cre*, The Jackson Laboratory stock number 004781)⁵⁷; *Nrp1*^{fl/fl}; *Rosa26*^{LSL-RFP/+}; *Cx3cr1*^{Cre-ERT2/+} (*RM*^{RFP-ΔNrp1}) mice, a conditional transgenic mouse model with a selective deletion of *Nrp1* in tissue RM obtained by crossing mouse with *Nrp1* gene flanked by LoxP sequences (*Nrp1*^{tm2Ddg/J}, *Nrp1*^{fl/fl}, The Jackson Laboratory stock number 005247)⁵⁶ with mouse with a cre recombinase under the *Cx3cr1* promoter (*Rosa26*^{LSL-RFP/+}; *Cx3cr1*^{Cre-ERT2/+}, *RM*^{RFP} mice).⁴⁹ To induce cre recombinase, *RM*^{RFP-ΔNrp1} mice were treated with 5 mg of tamoxifen (Sigma Aldrich) in 150 μ l sunflower oil (Sigma Aldrich) by oral gavage on 5 consecutive days, followed by 2 weeks of no treatment (washout) before further manipulation. All mice were backcrossed on C57BL/6J background and purity of the strain was routinely controlled by using the 128 SNPs MAX BAX Complete Background Analysis Panel (The Jackson Laboratory). For all the transgenic lines, WT mice generated within the same colony were used as aged and sex matched controls.

Cardiac pressure overload

Cardiac pressure overload was induced in mice anesthetized with a mixture of ketamine/xylazine (100/5 mg/kg), by performing TAC between the left carotid and the truncus anonymus, as previously described.^{14,58,59} In the study design we used trans-stenotic pressure gradient ranging from 85 to 105 mmHg as inclusion criteria of our cohorts of mice. Furthermore, the pressure gradient was monitored during each session of echocardiographic follow up analysis, in order to exclude that the challenge imposed on the LV could diminish over time, because of technical issues. Control mice (Sham) underwent the same surgical procedure but without realizing the stenosis.

Splenectomy

Splenectomy was performed 2 weeks before TAC or sham surgery in mice anesthetized with isoflurane (5% for induction and 1.5% for maintenance, supplemented with 1 L/min oxygen) as previously described.²⁴ To isolate and remove the spleen, the abdominal cavity was opened, and splenic vessels were cauterized. In control mice, the abdominal cavity was opened as well, but without removing the spleen.

Spleen Transplantation

Spleen transplantation was performed by concomitantly preparing donor and recipient mice, as previously described.²⁴ In brief, donor mice were anesthetized with a mixture of ketamine/xylazine (100/5 mg/kg) and heparin was intravenously injected. The spleen was exposed through a longitudinal incision in the abdomen and the splenic artery connected to vascular anastomosis was clamped before organ explant. At the same time, the recipient mouse was anesthetized with isoflurane (5% for induction and 1.5% for maintenance, supplemented with 1 L/min oxygen). Mice were subjected to an incision in the abdomen to expose the spleen and vasculature. The splenic artery and the vein of the recipient mouse were clamped, and the spleen was isolated and removed. Using a 10.0 suture thread (Premilene, Braun) an anastomosis was created between donor and recipient splenic veins and arteries. The clamp was removed to restore blood flow. Recovery of mice was monitored for the following 4 weeks,²⁴ before subjecting them to TAC-induced pressure overload and to allow the re-growth of the splenic innervation, which is functional, yet less structurally organized.

Surgical removal of the celiac ganglion (CGX)

The surgical removal of the left celiac ganglion was performed concomitantly or 2 weeks after TAC procedure, as indicated in schematics of the experiments (Figure S4). Mice were anaesthetized with isoflurane (5% for induction and 1.5% for maintenance, supplemented with 1 L/min oxygen). A midline laparotomy was applied, and aorta and celiac arteries were isolated. Once identified, the celiac ganglion was removed, taking care to avoid damage of the surrounding vessels and tissues. At the end of the surgical procedure, tissues were carefully repositioned into the abdominal cavity. The incision was sutured with absorbable thread. In control mice, the celiac ganglion area was exposed, and both the aorta and the celiac arteries were isolated, without removing the ganglion.

Surgical removal of the cervical ganglion (CerGX)

The surgical removal of the cervical ganglion was performed 1 week before TAC procedure in order to obtain a local myocardial SNS denervation. Mice were anaesthetized with isoflurane (5% for induction and 1.5% for maintenance, supplemented with 1 L/min oxygen). A vertical incision on the neck was made and the sternocleidomastoid muscle was lifted and moved aside with placeholders to allow a clear visibility of the carotid artery. The cervical ganglion, placed behind the carotid bifurcation, was exposed moving the external carotid artery with a 90° angled forceps and then was completely extracted cutting preganglionic and postganglionic branches. Moreover, the superior cervical ganglion was removed on the contralateral side for a complete denervation of cardiac tissue from sympathetic fibers. In control mice, the cervical area was exposed without removing ganglia.

Celiac vagotomy

Surgical unilateral celiac vagotomy was performed via a cervical midline incision that exposed the left vagus trunk, which was cut with forceps at the distal end of the coeliac branch of the vagus nerve. Vagus nerve was exposed while preparing the mouse for the electrophysiological recording. After the acquisition of two SSNA time bins, the celiac vagus nerve was transected, while SSNA recording continued for at least two additional time bins.³²

Ultrasound Imaging

Ultrasonographic analysis was performed with Vevo2100 (Visualsonics, Fujifilm) equipped with 40 and 15 MHz transducers, as previously described.¹⁴ Mice were anesthetized with isoflurane (3.5% for induction and 0.5%–1% for maintenance, supplemented with 1 L/min oxygen) and fixed on a heated pad, allowing the continuous monitoring of physiological parameters. In order to obtain the parasternal short axis projection, the thoracic area was shaved, and the 40 MHz ultrasound transducer was placed on the left side of anterior mediastinum. LV function was assessed on left ventricular M-mode images by applying the Teichholz formula and on apical 4 chambers view for diastolic evaluation. The aortic arch was visualized by 15 MHz ultrasound transducer placed on the right side of the upper anterior mediastinum, in correspondence of the TAC ligation, to measure the systolic trans stenotic gradient by echo Doppler. All images were acquired at a heart rate of at least 600 ± 50 bpm (beats per minute) and processed with the VevoLAB software by two independent raters.

In vivo administration of recombinant PIGF

Mice subjected to splenectomy have been treated by intraperitoneal injection of 1,5 µg/Kg body weight of recombinant PIGF (rPIGF) (R&D Systems) and with NaCl 0.9% as vehicle control as previously described.¹⁴ Follow up analysis of cardiac remodeling has been performed by echocardiography.

Non-invasive ultrasound-guided injection of AAV2/retro-CAG-TdTomato

Mice were anesthetized with isoflurane (3.5% for induction and 0.5%–1% for maintenance, supplemented with 1 L/min oxygen) and fixed on a heated pad as described above. Injection syringe with a 30G needle was positioned on a support allowing the correct orientation. The needle was aligned with the ultrasound probe and, by the aid of live echocardiographic imaging, was leaded in the mid portion of the LV anterior wall. 100 µl of AAV2/retro-CAG-TdTomato virus (1×10^{11} vg/ml) were directly injected and mice recovery was monitored for the following 3 weeks before culling them for immunofluorescence analysis.

Electrophysiological recordings

Mice were anaesthetized with isoflurane (5% for induction and 1.5% for maintenance, supplemented with 1 L/min oxygen).^{25,32,41} For SSNA recordings, after performing an abdominal incision to expose the splenic artery, the splenic nerve was isolated from the surrounding tissues and covered with a bipolar stainless-steel electrode as previously described.^{25,32,41} SSNA was continuously recorded for 1 hour, as was the arterial blood pressure from the femoral artery. Mice were then killed by an overdose of isoflurane and SSNA was recorded for a further 30 minutes to estimate the post-mortem residual activity.^{25,32,41} CVNA recordings were performed with the same experimental approach, exposing the celiac branch of the vagus nerve and placing the bipolar electrodes around it.^{25,32,41}

SSNA data were sampled at 4 kHz and analyzed using Lab Chart 7 (Spike Analysis Module). Signal was pre-processed by digital filtering of the electrical cord current using a 50 Hz notch filter and by a 300–1,000 Hz band-pass filter to highlight the frequencies of interest, expressing the final signal in μV . Splenic nerve spikes were identified as spikes with an intensity above the background noise threshold, measured in post-mortem acquisition, during a 10-minutes window starting from the electrodes' silicone isolation. Spike count was defined as the total number of spikes above the threshold intensity level.³²

The CVNA data were sampled and analyzed using Lab Chart 7 (Spike Analysis Module) and MATLAB (MathWorks) as previously described,²⁵ using the same settings as for the splenic nerve but digitally filtered by a narrower 300–550 Hz band-pass filter, to avoid high-frequency activity and noise. The obtained signal was integrated with a time-constant decay of 0.1 second to sum up the single-spike contribution to each burst. The integrated signal was processed using a custom MATLAB script to perform a peak analysis as previously described.²⁵ CVNA was quantified as the average bursts measured in two consecutive 10-minutes windows starting from the electrodes' silicone isolation.

Tissue isolation for histological analyses

For histological and immunofluorescence analyses, mice were anesthetized with ketamine/xylazine (100/5 mg/kg) and then culled to isolate the spleen, the nodose ganglion, the brain and the heart. The spleen and the nodose ganglion were embedded in optimal cutting temperature compound on dry ice. Serial 25 μm sections from spleens and serial 16 μm sections from nodose ganglion were obtained by using a cryostat microtome (Leica 1950CM, Leica Microsystems). Hearts were removed after diastolic arrest and embedded in paraffin. Hearts' sections of 10 μm were obtained by a microtome (Leica RM2255, Leica Microsystems). Brains were removed and immersed in fixative for 4 hours at 4°C and then cryoprotected in 20% sucrose overnight at 4°C. 30 μm free-floating frozen sections were cut using a cryostat microtome (Leica 1950CM, Leica Microsystems).^{60,61}

Immunofluorescence analyses

Spleens' sections were stained in blocking solution (serum 5% and X-100 Triton 0.25%) as follows: PIGF was stained with a rabbit anti-mouse primary antibody (1:250, Abcam), recognized by a horse anti-rabbit biotinylated antibody (1:200, Vector Laboratories) conjugated to Alexa Fluor 488 streptavidin (1:200, Invitrogen). ERT-R7 splenic fibroblasts were identified with a primary rat anti-mouse antibody (1:200, Origene) and a Cy3-conjugated donkey anti-rat secondary antibody (1:200, Jackson ImmunoResearch); CD169⁺ metallophilic macrophages were stained with a rat anti-mouse primary antibody (1:100, Biorad) and an Alexa Fluor 488-conjugated donkey anti-rat secondary antibody (1:200, Jackson ImmunoResearch); TH noradrenergic fibers were recognized by using a sheep anti-mouse primary antibody (1:800, Millipore) and a Cy3-conjugated donkey anti-sheep secondary antibody (1:200, Jackson ImmunoResearch). Hearts' sections were stained in blocking solution (serum 5% and X-100 Triton 0.20%) as following: capillaries were stained with Isolectin GS-IB4 conjugated to Alexa Fluor 488 (1:200, Invitrogen) overnight at 4°C; TH noradrenergic fibers were recognized by rabbit anti-mouse primary antibody (1:800, Millipore) and a Cy3-conjugated donkey anti-rabbit secondary antibody (1:200, Jackson ImmunoResearch). Slides were then counterstained with DAPI (1:2000, Invitrogen) and coverslipped with DABCO (Sigma-Aldrich).

Nodose ganglion and brain sections were analyzed by visualizing the spontaneous fluorescence of cells infected by the virus carrying the TdTomato reporter. Sections from nodose ganglion were post-fixed in 10% neutral buffered formalin at 4 °C for 15 minutes and washed in PBS, then incubated for 2 hours in blocking solution (serum 5% and X-100 Triton 0.2% in PBS). A rabbit anti-beta III Tubulin antibody (1:250, Abcam) was used to mark cytoskeletal proteins of nodose ganglion cells. Sections were washed in PBS and incubated with secondary antibody Alexa Fluor 488-conjugated donkey anti-rabbit (1:200, Jackson ImmunoResearch). Slides were then counterstained with DAPI (1:2000, Invitrogen) and coverslipped with DABCO (Sigma-Aldrich). Brain sections were stained with DAPI (1:2000, Invitrogen) and coverslipped with DABCO (Sigma-Aldrich).

Tissue sections were scanned using a Zeiss 780 confocal laser microscope equipped with a Zeiss ECPLAN-NEOFLUAR 5x/0.16 objective, Zeiss ECPLAN-NEOFLUAR 10x/0.30 M27 objective and ECPLAN-NEOFLUAR 20x/0.50 M27 (Carl Zeiss Microimaging Inc.). We used a 405 Diode laser to excite DAPI, a 488 nm argon laser to excite Alexa Fluor 488 and a 543 HeNe laser to excite Cy3.^{24,32,33}

Brain sections for the evaluation of activated FOS⁺ neurons were analyzed as previously described.⁴¹ In detail, brains were extracted, post-fixed in 10% neutral buffered formalin at 4 °C overnight, and cryoprotected in 20% sucrose at 4 °C. Twenty-five μm -thick coronal sections were cut on a freezing microtome. Sections were washed in PBS, then incubated for 1 hour in blocking solution (0.5% BSA and 0.25% Triton X-100 in PBS). Primary rabbit anti-c-FOS (1:5000, Abcam) antibody was incubated overnight in blocking solution. Sections were washed in PBS and incubated with secondary antibody Alexa Fluor 594-conjugated donkey anti-rabbit (1:1000, Abcam). Sections were washed, mounted on slides, cover-slipped, and visualized on a Zeiss Axiomanager.D2 microscope. Images were captured using a Coolsnap HQ1 camera through Micromanager software v1.4.23.

Immunohistochemical analysis

Hearts' sections were deparaffinized, rehydrated and then underwent to standard protocol for picosirius red staining for the identification of collagen in cardiac tissues.¹⁴ The Picosirius Red Solution was prepared by adding 0.5 g of Sirius red F3B to 500 ml of picric acid. Slides with sections of hearts were immersed on the Picosirius Red Solution for 1 hour and then washed in twice in acidified water, previously prepared by adding 2.5 mL of acetic acid in 500 mL of distilled water. After removing the excess of water, slides were dehydrated, cleared in xylene and mounted on a quick-hardening mounting medium (Eukitt - Sigma-Aldrich, 03989). Images were acquired by an optical microscopy (Leica LMD7).

ELISA for determination of PIGF and IGF-1

After transcardial perfusion, spleens and hearts were isolated and immediately frozen in liquid nitrogen for protein extraction. To collect serum, blood samples were allowed to clot for 1 hour at room temperature and then centrifuged for 15 minutes at 2000 x g at 4°C. After centrifugation, serum aliquots were immediately stored at -20°C. PIGF amounts in spleen and serum were measured by a high sensitivity ELISA kit (R&D Systems MP200), following manufacturer's instructions as previously described.^{24,33} IGF-1 amounts in the heart were measured by The Quantikine Mouse/Rat IGF-1 ELISA kit (R&D Systems MG100), following manufacturer's instructions as previously described.²⁷

Tissue isolation and cells staining for flow cytometry analysis

Mice were anesthetized with a mixture of ketamine/xylazine (100/5 mg/kg) and then culled to collect the heart, after washing out circulating cells and blood with cold PBS. Atria were excised and removed; cardiac tissue was placed in a 60 mm dish containing 50 µl of cold PBS and finely chopped. The minced heart was transferred into a 2 ml microcentrifuge tube pre-filled with 800 µl of Dulbecco's Modified Eagle Medium (DMEM) (Gibco 21969-035) and 650 µl of digestion cocktail, composed by 450 U/ml of Collagenase Type I (Sigma-Aldrich C0130), 60 U/ml of Hyaluronidase Type I-S (Sigma-Aldrich H3506), 60 U/ml of DNase I (Sigma-Aldrich D5025) in DMEM. The heart was digested in a thermomixer at 37°C for 1 hour at 750 rpm. After digestion, the tissue sample was vortexed for 20 seconds and immediately placed on ice. Using a 1 ml pipettor, the tissue was pipetted up and down 30 times until obtaining a homogeneous sample that was added to a 40 µm nylon strainer placed on a 50 ml conical tube and pre-wet with 1 ml of cold HBB buffer, containing Hank's Balanced Salt Solution HBSS (Gibco 24020-091) supplemented with 2% heat inactivated FBS (Gibco 10082-147) and 0.2% of BSA. The strainer with the homogenized sample was further washed with 12 ml of HBB buffer. The sample was transferred to 15 ml conical tube and centrifuged at 300 x g for 5 minutes at 4°C. The blood cells were lysed with 1 ml of BD Lysing buffer 1X (BD PharmLyse 555899) for 5 minutes at room temperature. 8 ml of HBSS were added to block lysis, and the sample was then centrifuged at 300 x g for 5 minutes at 4°C. The supernatant was discarded, the pellet was resuspended in 1 ml of FACS buffer (PBS supplemented with 2% heat inactivated FBS and 2 mM EDTA) and cell number was assessed by trypan blue on an automated counter (Countess, Life Technologies) and resuspended in FACS staining buffer.

Flow cytometry staining and gating strategies

The single cell suspension obtained from the heart was preincubated with anti-CD16/32 Fc receptor (1:100, BD Pharmingen) and True-Stain Monocyte Blocker (1:20, Biolegend) to block nonspecific binding for 10 minutes at room temperature and then incubated with a combination of fluorochrome-conjugated primary monoclonal antibodies (listed in [key resources table](#) and mixed accordingly to the "Gating strategy for cardiac monocytes and macrophages" subparagraph) in 50 µl of BD Brilliant Stain buffer (BD Horizon 566349) for 30 minutes at 4°C in the dark in a final staining volume of 150 µl. Cells were washed, resuspended in 300 µl of FACS buffer and filtered through a 40 µm nylon strainer before acquiring the samples with a FACSCelesta equipped with a FACSDiva Software (BD Bioscience) or with a multispectral Cytex Aurora equipped with SpectroFlo software (Cytex). Data were analyzed with FlowJo Software v10.8.1 (FlowJo, LLC).

For proliferation experiment, 100 µl of Bromodeoxyuridine (BrdU) (10 mg/ml, BD Pharmingen 550891) was injected intraperitoneally (i.p.) 12 hours before heart harvest. To detect intracellular BrdU, the BD Bioscience Cytofix/Cytoperm (BD Cytofix/Cytoperm Plus 555028) protocol was used as previously described.¹⁶ After cell surface staining with antibodies listed in [key resources table](#) and mixed accordingly to the "Gating strategy for cardiac monocytes and macrophages" subparagraph, cells were washed and resuspended in 250 µl Fixation/Permeabilization solution, washed with BD Perm/Wash buffer 1X and incubated overnight. DNA was digested for 1 hour 37°C with 100 µl of DNase (300 µg/ml, Sigma-Aldrich D4513). After incubation, cells were washed with BD Perm/Wash buffer 1X and labelled with anti-BrdU antibody (1:10, BD Pharmingen) in a final staining volume of 50 µl of Perm/Wash buffer 1X for 30 minutes at room temperature in the dark. Cells were washed, resuspended in 300 µl of Perm/Wash buffer 1X and filtered through a 40 µm nylon strainer before acquiring the samples with FACSCelesta equipped with FACSDiva Software (BD Bioscience). Data were analyzed with FlowJo Software v10.8.1 (FlowJo, LLC).

For all the experiments, compensation was developed using single staining controls and compensation beads (BD CompBeads 552845, 552843).

Gating strategy for cardiac monocytes and macrophages (Figures S2, S6, and S7). Cells were gated to identify total CD45⁺ leukocytes, doublets were excluded, and live cells were analyzed using forward scatter (FSC) and side scatter (SSC) to live/dead exclusion. Total leukocytes were parsed to exclude Ly6G⁺ neutrophils and identify the Ly6G⁺CD11b⁺ monocytes/macrophage population. CD11b⁺ cells were further gated by CD64 expression to identify CD11b⁺CD64⁺ cells and CD11b⁺CD64⁺ macrophages. CD11b⁺CD64⁺ cells were then stratified into Ly6C^{lo} and Ly6C^{hi} monocytes. CD11b⁺CD64⁺ (Mac) cardiac macrophages were gated to identify Timd4⁺Ly6C^{lo} and Timd4⁺Ly6C^{lo} RM and Timd4⁺Ly6C^{hi} replenished/recruited macrophages.^{16,17,28} Where indicated in figure legends, cardiac RM were identified by red fluorescent protein (RFP) expression (Figure S7), and/or further identified by Lyve-1, Nrp1 and CD206 expression or BrdU incorporation. Briefly, total CD11b⁺CD64⁺ cardiac macrophages were stratified by Ly6C, Timd4 and Lyve-1 to identify Ly6C^{lo}Timd4⁺Lyve-1⁺ RM and Ly6C^{lo}Timd4⁺Lyve-1⁺CD206⁺ resident pro-fibrotic subpopulation. To evaluate the expression of Nrp1 in macrophage subpopulations, we set the positive fraction by gating the negative population with cells isolated from *Nrp1^{fl/fl};Lyz2^{cre/+}* mice and hence lacking NRP1 in the myeloid lineage (Figure S7). Also, BrdU incorporation was evaluated in Ly6C^{lo}Timd4⁺Lyve-1⁺ cardiac RM (Figure S6).

Data analysis of scRNA-seq

The package Seurat (v3.1) was used for all scRNA-seq analyses using R 3.61.^{50,51} Genes not detected in a minimum of three cells were removed. Low-quality cells with less than 200 expressed genes were excluded. Cells expressing a high number of genes (>4000–6000)

were considered as putative doublets or multiplets and were removed. Dead or lysed cells were removed by exclusion of cells with a high percentage of transcripts mapping to mitochondrial genes (>20%–30%). Sham and TAC datasets were first pre-processed and filtered individually, then merged for all subsequent analyses using the “merge” function in Seurat. To remove technical variation while preserving biological variation, data was log normalized. Highly variable features were selected (3000 by default) using the variance-stabilizing transformation (vst) method. Mitochondrial gene percentage and the number of counts (nCount_RNA) were regressed out. Dimensionality reduction was performed using principal component analysis (PCA) and the most statistically significant PCs were chosen for subsequent clustering as determined by examination of the standard deviation of each principal component depicted on an elbow plot. Graph-based clustering was performed using the FindNeighbors and FindClusters functions. Non-linear dimensionality reduction and visualization was performed using Uniform Manifold Approximation and Projection (UMAP). In order to assess the finer division of cardiac macrophages, we assessed the parent cluster separately and increased resolution. Clusters were identified and annotated based on differential gene expression testing using the Wilcoxon Rank Sum Test. In particular, we used the following parameters in the FindAllMarkers function: min.pct: 0.2; logFC threshold: 0.2; adjusted p value <0.05.

Statistical analysis

All data were analyzed by Prism 7 and 9 (GraphPad) and SPSS 23 (IBM). Comparisons between two experimental groups with single time point were performed by two-tailed Student’s t-test. Comparison between multiple experimental groups were performed by one-way ANOVA with Tukey post hoc test. Analyses with multiple factors were analyzed by either two-way ANOVA or repeated measures ANOVA, with either Sidak or Tukey post hoc test as appropriate and indicated in Figure legends.

HUMAN STUDIES

Ethics committee

The study was approved by the local ethics committee of the Jagiellonian University (Approval No. 1072.6120.162.2019 and 1072.6120.225.2019). Subset of patients enrolled in the two studies previously published by our group^{62,63} that received a blood sampling, blood pressure measurements and echocardiography were prospectively recruited between November 2014 and December 2020 in the Heart and Brain research program at I.R.C.C.S. Neuromed (NCT03986957) and as part of a case-control study (NCT02310217). Written informed consent was obtained from all subjects.

Gene expression measurements in cardiac biopsies

In a subset of patients, depending on clinical availability, typically two-three cardiac biopsies were obtained from the left ventricle. Collected cardiac tissue was stored in RNAlater stabilization solution (Ambion, Thermo Fisher Scientific) until RNA isolation. The tissue was homogenized for 20 min in TRI Reagent Solution (Thermo Fisher Scientific) using the TissueLyser LT bead mill (Qiagen, USA). Total RNA was isolated from the samples using Direct-zol RNA Miniprep kit (Zymo Research R2052) according to the manufacturer’s protocol. Reverse transcription was performed using 500 ng of RNA using High Capacity cDNA reverse transcription kit (Applied Biosystems, USA 4368814). Real-time PCR reactions were performed on the 7900HT instrument (Applied Biosystems, USA) using commercially available TaqMan assays for NRP1 (Hs00826128_m1) and CD68 (Hs02836816_g1). Data were normalized to levels of Eukaryotic Translation Elongation Factor 2 (EEF2) (Hs00157330_m1) mRNA, and then dCT was calculated and averaged between cardiac biopsies for each of the patients. N numbers reported represent individual patients.

Statistical analysis

The normality of variables distribution was checked with the Shapiro-Wilk test. Continuous variables with normal distribution were compared using the Student’s t-test. Continuous variables with non-normal distribution were compared using Mann-Whitney test. Categorical variables were compared using the χ^2 -squared test. The continuous variables are presented as mean \pm SD or median (Q1; Q3), whereas the categorical variables are presented as numbers and percentages.

Pearson’s correlation was performed to analyze the correlation between Nrp1 mRNA expression and CD68 mRNA expression. A P value below 0.05 was considered statistically significant. All analyses were performed using IBM SPSS Statistics (New York, United States) package (version 28.0.1.0) and graphs were drawn using Graph-Pad Prism v9.1.0.

Immunofluorescence analyses of cardiac biopsies

LV of myocardium from HTN-HD patients were collected and embedded in OCT. Cryosections of 20 μ m were obtained from each sample by using the cryostat (Leica CM 1950). Primary antibodies used to stain cardiac tissues were mouse anti-CD68 (Biorad MCA5709; 1:100); mouse anti-Neuropilin1 (Santa Cruz sc-5307; 1:100) and rabbit anti-CCR2 (Abcam ab32144; 1:200). The following secondary antibodies were used: F(ab’)2 fragment antibody (Jackson ImmunoResearch; 1:200) and secondary antibodies conjugated to Alexa Fluor 647 (Jackson ImmunoResearch; 1:100), Alexa Fluor 488 (Jackson ImmunoResearch; 1:200) and Cy3 (Jackson ImmunoResearch; 1:200). Nuclei were counterstained with DAPI (Invitrogen, 62248; 1:2000) and slides coverslipped with DABCO mounting medium (Sigma-Aldrich).

Quantification of circulating amount of PIGF

PIGF serum amount were measured by a high sensitivity ELISA kit (Abcam ab100629), following manufacturer’s instructions.